SDAC-TR-77-12

LEVEL

THE EFFECTS OF SPALL ON
m_b AND M_s

P.A. SOBEL

Seismic Data Analysis Center

Teladyne Geotech; 314 Montgomery Street, Alexandria Virginia 22314

04 APRIL 1978

79 07 24 082

REPORT DOCUMENTATION PAGE		READ INSTRUCTIONS BEFORE COMPLETING FORM
1. REPORT NUMBER SDAC-TR-77-12	2 GOVT ACCESSION NO.	3 RECIPIENT'S CATALOG NUMBER
4. TITLE (and Subtitle) THE EFFECTS OF SPALL ON m_b AND M_s		5 TYPE OF REPORT & PERIOD COVERED Technical 6 PERFORMING ORG REPORT NUMBER
7. AUTHOR(s) P. A. Sobel		8 CONTRACT OR GRANT NUMBER(s) F08606-78-C-0007
9 PERFORMING ORGANIZATION NAME AND ADDRESS Teledyne Geotech 314 Montgomery Street Alexandria, Virginia 22314		10 PROGRAM ELEMENT PROJECT TASK AREA & WORK UNIT NUMBERS T/8709/B/ETR
11. CONTROLLING OFFICE NAME AND ADDRESS Defense Advanced Research Projects Agency Nuclear Monitoring Research Office 1400 Wilson Blvd., Arlington, Virginia 22209		12 REPORT DATE 04 April 1978
		13 NUMBER OF PAGES 60
14. MONITORING AGENCY NAME & ADDRESS(If different from Controlling Office) VELA Seismological Center 312 Montgomery Street Alexandria, Virginia 22314		15 SECURITY CLASS (of this report) Unclassified
		15a DECLASSIFICATION DOWNGRADING SCHEDULE

16. DISTRIBUTION STATEMENT (of this Report)

APPROVED FOR PUBLIC RELEASE; DISTRIBUTION UNLIMITED.

17 DISTRIBUTION STATEMENT (of the abstract entered in Block 20, if different from Report)

18. SUPPLEMENTARY NOTES

Author's Report Date 10/26/77

19 KEY WORDS (Continue on reverse side if necessary and identify by block number)

Underground Nuclear Explosion
Spall
Magnitude-Yield
Explosion Energy

20 ABSTRACT (Continue on reverse side if necessary and identify by block number)

This study examines near-field observations of spalling, a phenomenon associated with most underground nuclear explosions, and attempts to estimate its effects on m_b and M_s. Observations of spall on near-field accelerometers and partical velocity records were used to examine possible relationships between radius of spallation, estimated spall thickness, maximum height attained by spall at the surface, shot depth of burial and yield.
Estimates of pP-P and P_{SPALL}-P at teleseismic distances were calculated

from near-field measurements of uphole time and spall observations for 47 explosions. Spall energies relative to explosion energies were estimated assuming that a single spall closure was responsible for most observed surface displacements. Some calculated spall energies were larger than the explosion energy entering the spall region, suggesting that the method for calculating spall energy is in error. Relative spall energies compared to explosion energies for 42 NTS explosions located below the water table show no relationship to M_s residuals or strain release. Subsurface vertical accelerometer records show that spall energy is divided among several closures over a range of depths, the deeper formations closing before the shallower layers. The large observed spall pulses are due to closures closest to the gauge. The principal error in the spall energy calculations was, therefore, the assumption that the first spall closure contained most of the spall energy. The total spall energy, the sum of many spall closures, is probably much smaller than the spall energy calculated for a single spall closure. The subsurface accelerometer data show little, if any, spall energy leaving the source region, suggesting that spall has little effect on m_b and M_s at teleseismic distances.

THE EFFECTS OF SPALL ON m_b AND M_s

SEISMIC DATA ANALYSIS CENTER REPORT NO.: SDAC-TR-77-12

AFTAC Project Authorization No.:	VELA T/8709/B/ETR
Project Title:	Seismic Data Analysis Center
ARPA Order No.:	2551
Name of Contractor:	TELEDYNE GEOTECH
Contract No.:	F08606-78-C-0007
Date of Contract:	01 October 1977
Amount of Contract:	$2,674,245
Contract Expiration Date:	30 September 1978
Project Manager:	Robert R. Blandford (703) 836-3882

P. O. Box 334, Alexandria, Virginia 22313

APPROVED FOR PUBLIC RELEASE; DISTRIBUTION UNLIMITED.

ABSTRACT

This study examines near-field observations of spalling, a phenomenon associated with most underground nuclear explosions, and attempts to estimate its effects on m_b and M_s. Observations of spall on near-field accelerometers and particle velocity records were used to examine possible relationships between radius of spallation, estimated spall thickness, maximum height attained by spall at the surface, shot depth of burial, and yield.

Estimates of pP-P and P_{SPALL}-P at teleseismic distances were calculated from near-field measurements of uphole time and spall observations for 47 explosions. Spall energies relative to explosion energies were estimated assuming that a single spall closure was responsible for most of the observed surface displacements. Some calculated spall energies were larger than the explosion energy entering the spall region, suggesting that the method for calculating spall energy is in error. Relative spall energies compared to explosion energies for 42 NTS explosions located below the water table show no relationship to M_s residuals or strain release. Subsurface vertical accelerometer records show that spall energy is divided among several closures over a range of depths, the deeper formations closing before the shallower layers. The large observed spall pulses are due to closures closest to the gauge. The principal error in the spall energy calculations was, therefore, the assumption that the first spall closure contained most of the spall energy. The total spall energy, the sum of many spall closures, is probably much smaller than the spall energy calculated for a single spall closure. The subsurface accelerometer data show little, if any, spall energy leaving the source region, suggesting that spall has little effect on m_b and M_s at teleseismic distances.

TABLE OF CONTENTS

LIST OF FIGURES

LIST OF FIGURES (continued)

LIST OF TABLES

INTRODUCTION

Spalling is a phenomenon associated with most underground nuclear explosions. The compressional stress wave leaving the source is reflected at the Earth's surface and travels downward as a tensile stress wave. Where tensile stress exceeds compressive stress remaining in the upward travelling wave, plus stress due to the overburden and tensile strength of the rock, near-surface layers will physically part (Figure 1). The impact during closure of the spall gap produces a signal observed on near-field instruments. The purpose of this study is to estimate the effect, if any, of spall on teleseismic m_b and M_s measurements.

Estimated spall depth, spall radius, maximum height attained by spall, shot depth of burial, and yield were examined to determine any possible relationships between these parameters. Estimates of teleseismic $P_{SPALL}-P$ times were calculated from near-field accelerometer data for 47 explosions with observed spall. Spall and explosion energies were calculated and subsurface vertical accelerometer data examined to determine the amount of spall energy leaving the source region. This study demonstrates that assuming the first, and deepest, spall closure contains most of the spall energy is wrong and that calculations of spall energy cannot be based solely upon near-field surface measurements.

NEAR-FIELD MEASUREMENTS OF SPALL

An underground explosion produces spalling when the tensile stress wave reflected at the surface exceeds compressive stress remaining in the upward travelling wave, plus the stress due to the overburden and the tensile strength of the rock (Figure 1). The energy of the waves trapped in the formation causes the layers to ascend and spall is created. At the surface near an explosion, the first signal recorded is the pulse travelling upward from the explosion, t_0. The second signal, t_2, originates from the spall closure directly below the point of observation. Figure 2 shows the two ray paths schematically. The arrival time between t_0 and t_2 is denoted Δt. The first signal on the accelerometer trace is a positive pulse from the explosion followed by a free fall period of $-g$, and then a positive pulse from the spall closure.

In several already existing studies, investigators assume a constant spall layer thickness since no observations of lateral variations in spall thickness exist. The maximum height the layer is projected, S_{max}, is generally observed to be greater over the explosion, tapering off to zero at increasing distances from the source. The shape of spall height is assumed to be conical with sides concave upward as shown in Figure 3 (Eisler and Chilton, 1964).

Since the maximum observed surface displacement is greater than the S_{max} derived from displacement data both above and below the spall depth, additional spalling at other depths must be taking place (Eisler et. al., 1966). Several possible spall signals are recorded at the surface for some events and subsurface near-field instrumentation indicates several spall depths for some events. After the first spall is created, remaining parts of the stress wave may travel upward and downward to create more spalls above and below the first spall. The subsurface spalled region may have upper and lower bounds where the pulses erode to the point that spalling no longer takes

Eisler, J., and Chilton, F., 1964. Spalling of the Earth's surface by underground nuclear explosions, J. Geophys. Res., 69, 5285.

Eisler, J., Chilton, F., and F. Sauer, 1966. Multiple subsurface spalling by underground nuclear explosions, J. Geophys. Res., 71, 3923.
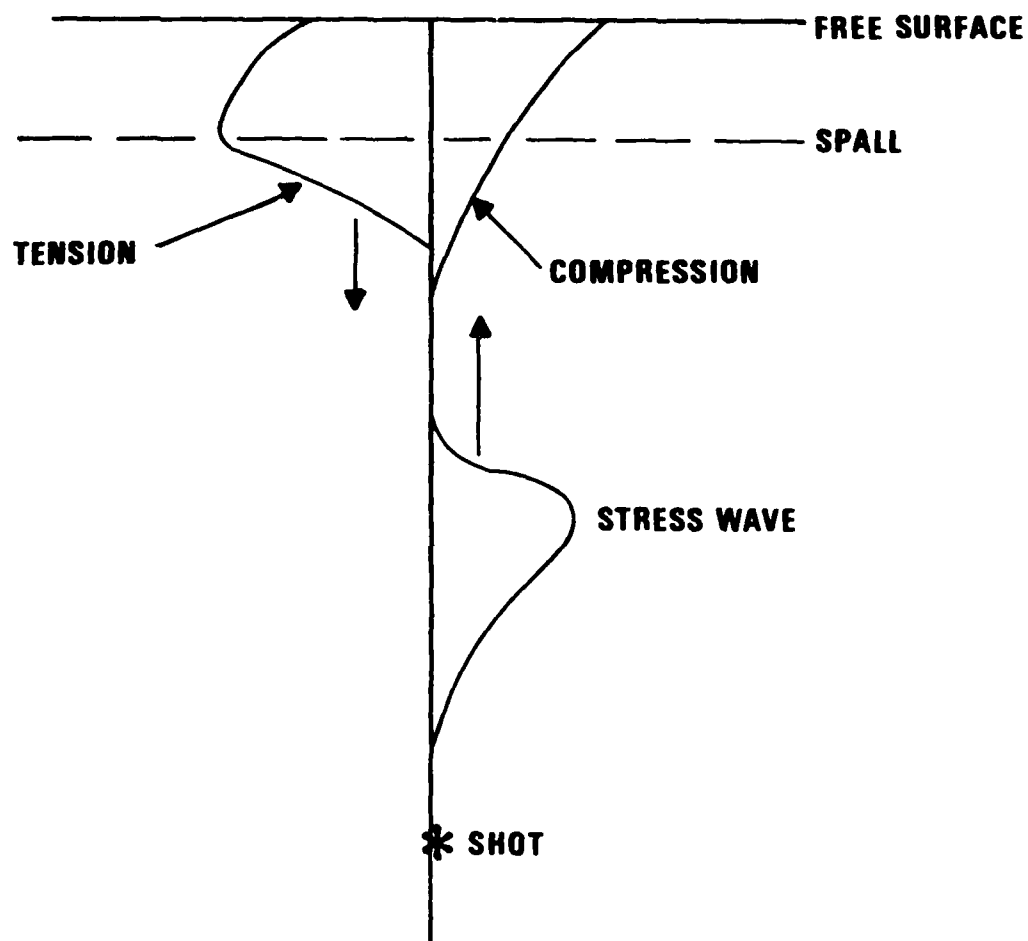
Figure 1. Generation of a spall by a compressional stress wave (Eisler and Chilton, 1964).

ACCELEROMETER

t_0 t_2 t_3

CROSS-SECTIONS OF RAY PATHS

r t_0 r t_2 t_3

TELESEISMIC P

TELESEISMIC P$_{SPALL}$

ARRIVAL TIME VERSUS RANGE

t

t_2

t_0

t_{UPHOLE}

0

0 r_0

r
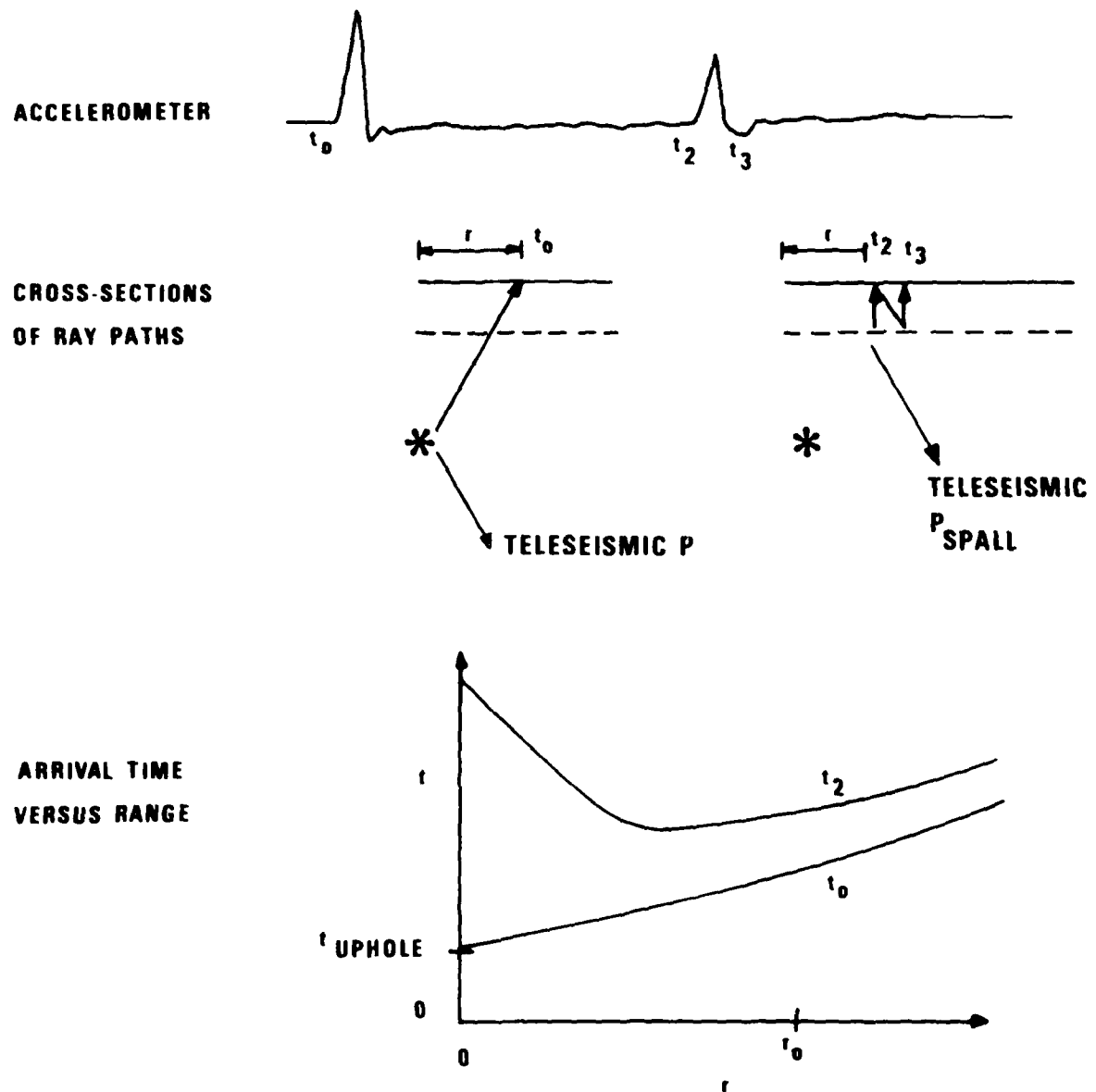
Figure 2. Direct ray and spall pulse recorded at the surface near an explosion.

- 10 -

GROUND SURFACE

S_{max}

S

✳ shot
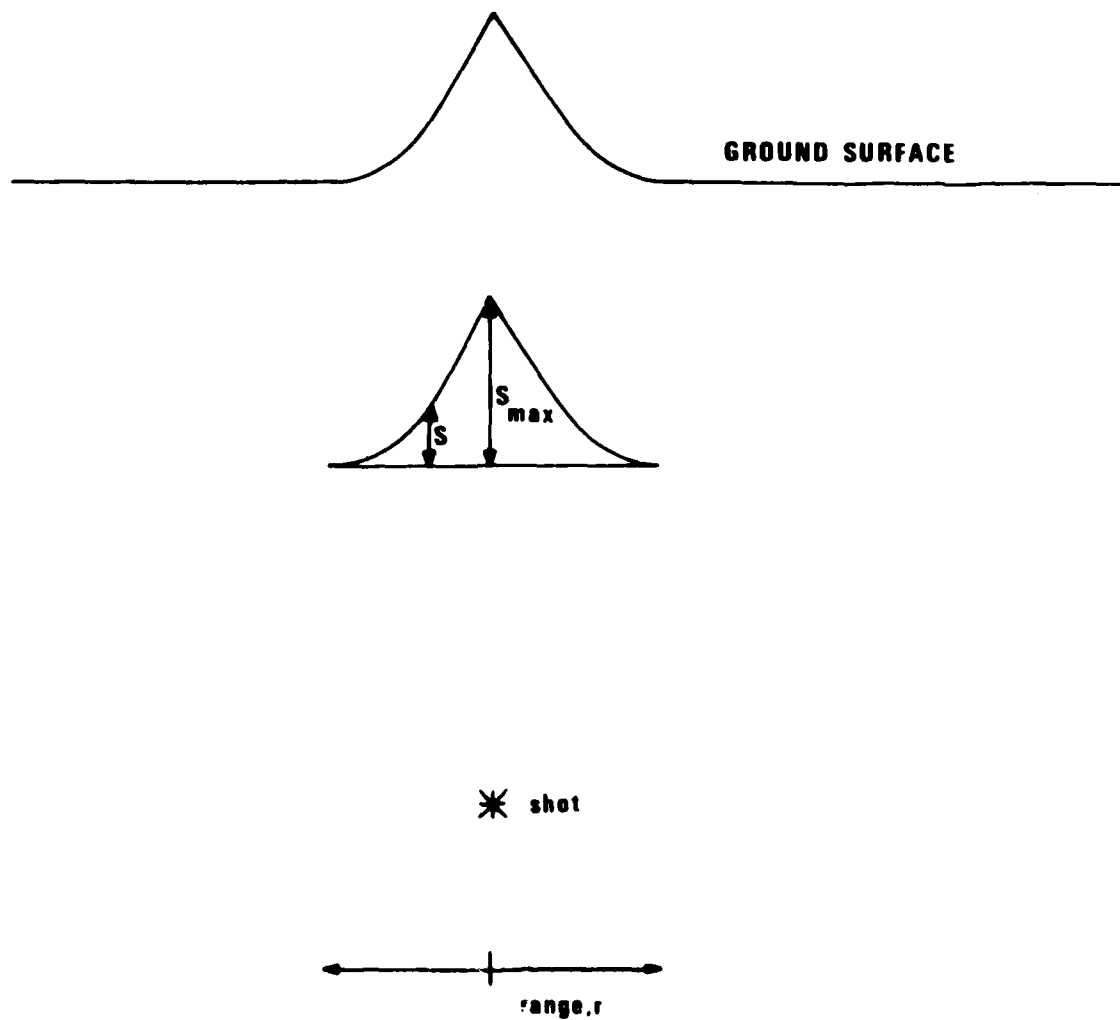
range,r

Figure 3. Variation of maximum height of projection
of spall layer(s) versus range(r)

- 11 -

place (Chilton et. al., 1966). The thicknesses of all the layers are assumed constant because no observations of their shapes exist.

Figure 4 shows several surface records for the explosion MILROW in the Aleutian Islands. Spalling signals were recorded out to 10,000 meters of horizontal range from the source. Vertical arrays of accelerometers showed zones of spall partings at 100 to 300 feet, 300 to 500 feet, and 500 to 1000 feet. A computer program that simulates velocities and stress profiles with time in the rock column indicated that a parting would occur at from 350 to 400 feet (Perret and Breding, 1972). The spall at this depth range was the first to close and produced the first and largest spall signal on the accel-erometers. Note that spall signals on accelerometer records are relatively large compared to the main phase from the explosion. The large signals occur because the source of the spall signal is directly under the accelerometer and it has travelled a smaller distance and is less attenuated than the explosion signal.

Perret, W., and D. Breding, 1972. Ground motion in the vicinity of an under-
    ground nuclear explosion in the Aleutian Islands: MILROW event, Sandia
    Laboratories, Research Report SC-RR-71-0668.
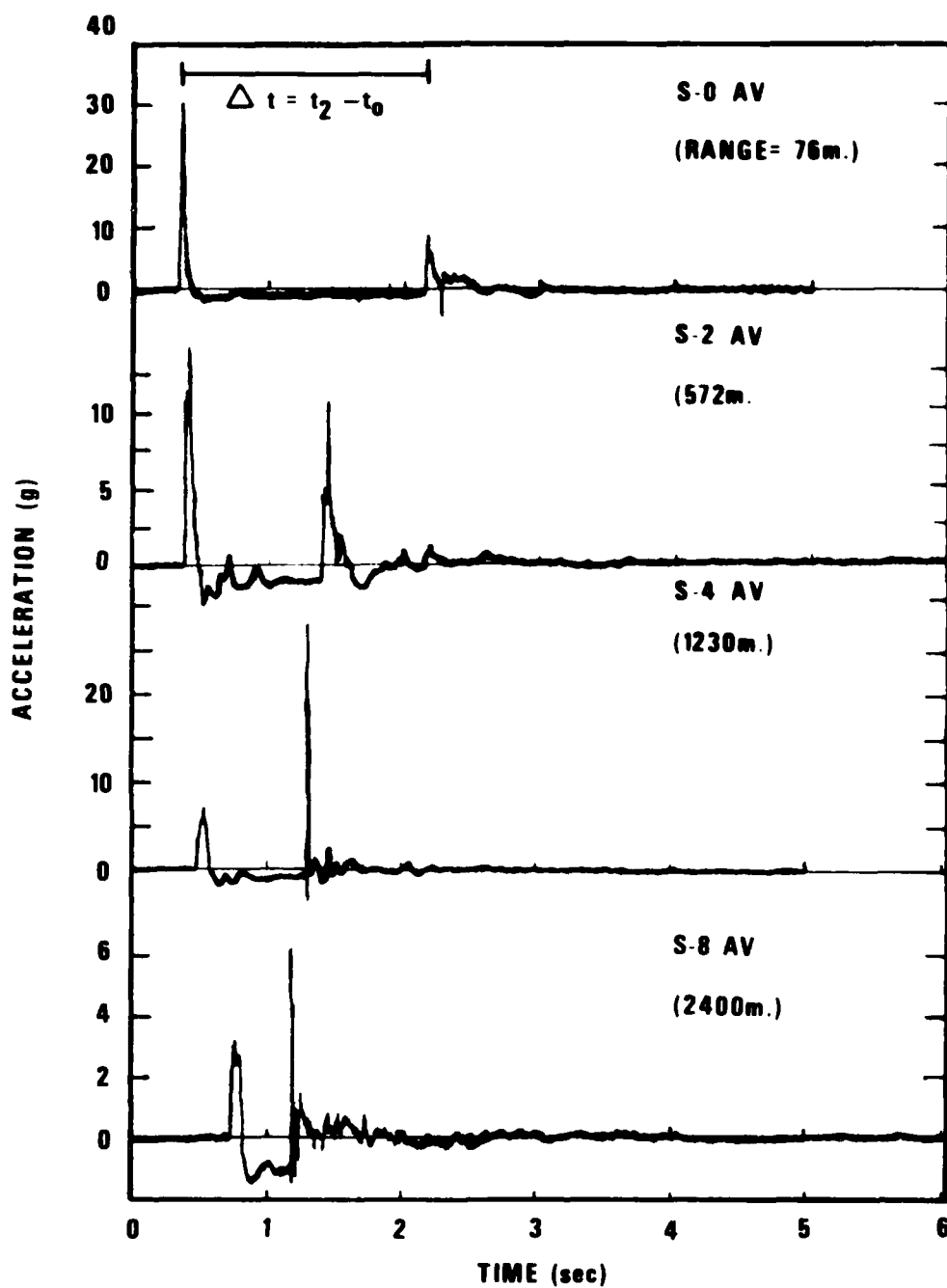
Figure 4. Surface accelerometer, particle velocity, and displacement data at various horizontal distances from the shot hole for the Aleutian Islands explosion MILROW.

- 13 -

Figure 4. (cont.) Surface accelerometer, particle velocity, and displacement data at various horizontal distances from the shot hole for the Aleutian Islands explosion MILROW.

- 14 -

Figure 4. (cont.) Surface accelerometer, particle velocity, and displacement data at various horizontal distances from the shot hole for the Aleutian Islands explosion MILROW.

- 15 -
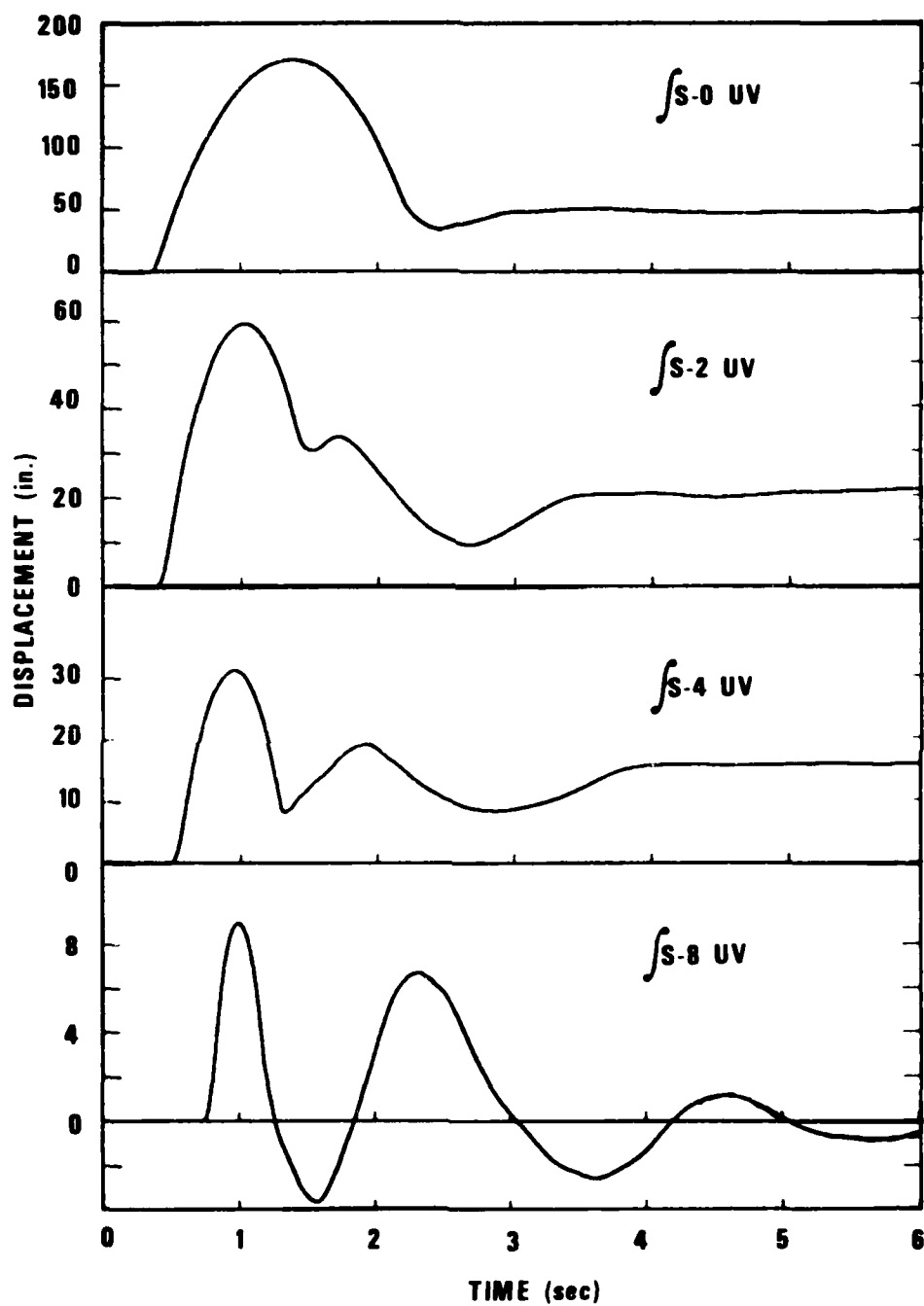
ESTIMATES OF SPALL PARAMETERS

Viecelli (1973) estimated the depth, height, and radial extent of spallation from near-field accelerometer records for seven NTS explosions and plotted these parameters against shot depth of burial and yield. The present study will add more data points to his figures from 47 explosions at NTS, as well as other test areas in Nevada, New Mexico, Mississippi and the Aleutians. These estimates of spall parameters will be used in a later section to determine the energy of the spall closure for a falling disc with parameters estimated from near-field surface accelerometer and particle velocity data.

The thickness of spall was determined from subsurface vertical accelerometer array data near the sources, observations of partings in boreholes, and determination of the arrival of the phase t_3, which is reflected off the spall layer (Figure 2). The first spall closure was assumed to contain most of the energy. The maximum height of the spall was observed by near-field vertical arrays or calculated theoretically from the observed maximum value of $\Delta t = t_2 - t_0$ at the surface and the acceleration of gravity g according to the formula

$$S_{max} = \frac{(\Delta t)^2 g}{8}$$

(Eisler and Chilton, 1964). The radial extent of spallation is defined as that horizontal range from the source where Δt becomes constant. For some explosions this condition was approached near the largest range measured and the radius of spallation is taken as the maximum horizontal range of measurement.

Viecelli, J., 1973. Spallation and the generation of surface waves by an underground explosion, J. Geophys. Res., 78, 2475.

In a few cases near-field vertical accelerometer data was available from Eisler (1967), Eisler and Chilton (1964), Eisler, Chilton and Sauer (1966), Perret (1968), Perret and Breding (1972), Viecelli (1973), and Weart (1962).

Eisler, J., 1967. Near-field spalling from a nuclear explosion in a salt dome, J. Geophys. Res., 72, 1751.

Perret, W., 1968. Free-filed particle motion from a nuclear explosion in salt, Part I, Vela Uniform Program, SALMON event, Sandia Laboratories, Report VUF-3012.

Weart, W., 1962. Particle motion near a nuclear detonation in halite, Bull. Seism. Soc. Amer., 52, 981.

In all cases Sandia Laboratory near-field particle velocity data, that D. Springer made available to the author at the Lawrence Livermore Laboratory, was used to determine values of Δt and ground displacement as a function of horizontal range. The Appendix includes this data for all horizontal ranges out to the radial extent of spallation. The surface particle velocity data listed times between the first and second zero crossing on the particle velocity records at several horizontal ranges for each explosion. When the particle velocity records were compared to the accelerometer data (Figure 4), these times were found to be equal to $0.5\Delta t$. Note in the appended material that peak displacements do not always decrease with increasing range for any given explosion. The conical approximation for the shape of S_{max} is not always valid, probably because of changing lithologies in the source region.

In most cases this study picked a larger spall radius for the explosions than the radius used in Viecelli's study. This discrepancy stems from the methods used in the two different studies to determine spall radius. Viecelli, as shown in Figure 2, uses the horizontal radius of the minimum arrival time of t_2 as the spall radius. He reasoned that where the t_2 arrival time was a minimum, the free fall time of the slab under that point was smallest. The Sandia Laboratory particle velocity data gave values of Δt and not values of t_2 and t_0 at various ranges from the source. The spall radius was established as the range where the time Δt became constant, assuming that beyond that range there was no spall under those observation points.

Figure 5 shows the thickness of spall versus explosion yield. In Figures 5 through 14 the dots are Viecelli's data points and the circles are from this study. Data points for this study are tabulated in Table I. Arrows connect the two data points where our data points differ from Viecelli's for the same explosions. The figures show the lines Viecelli used as best fits to his data and the least squares lines of best fit calculated when the new data points are added to the figures. The additional data points show more scatter than Viecelli's original set, a conclusion found in all the figures resulting from changing lithologies in the source regions. Viecelli's line in Figure 5 has a slope of 1/3. The present study also indicates the same relationship between spall thickness and yield, but the new best fit line has
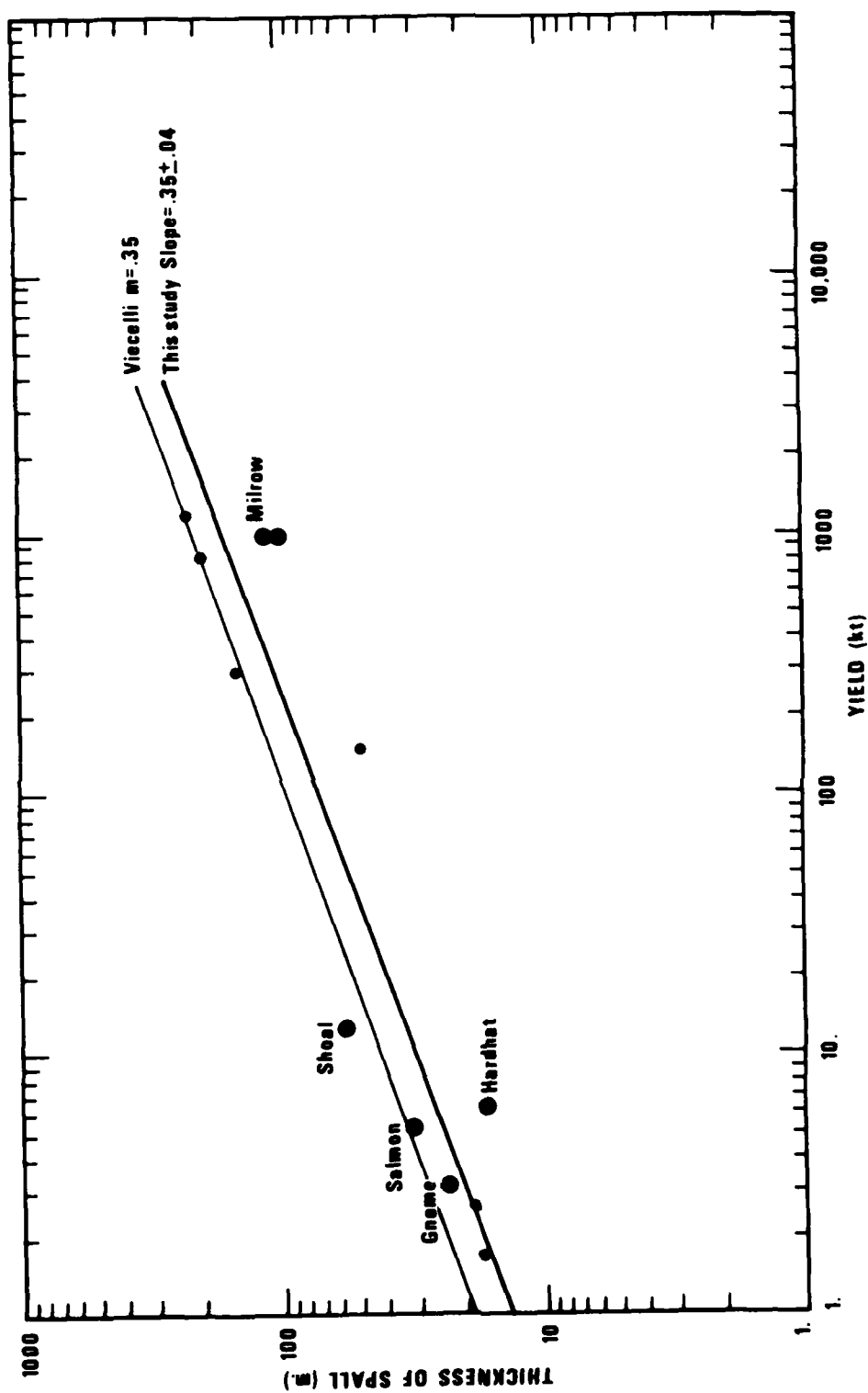
Figure 5. Thickness of spall vs. yield. In Figures 5 through 14 dots are data points from Viecelli (1973); circles are data points from the present study.
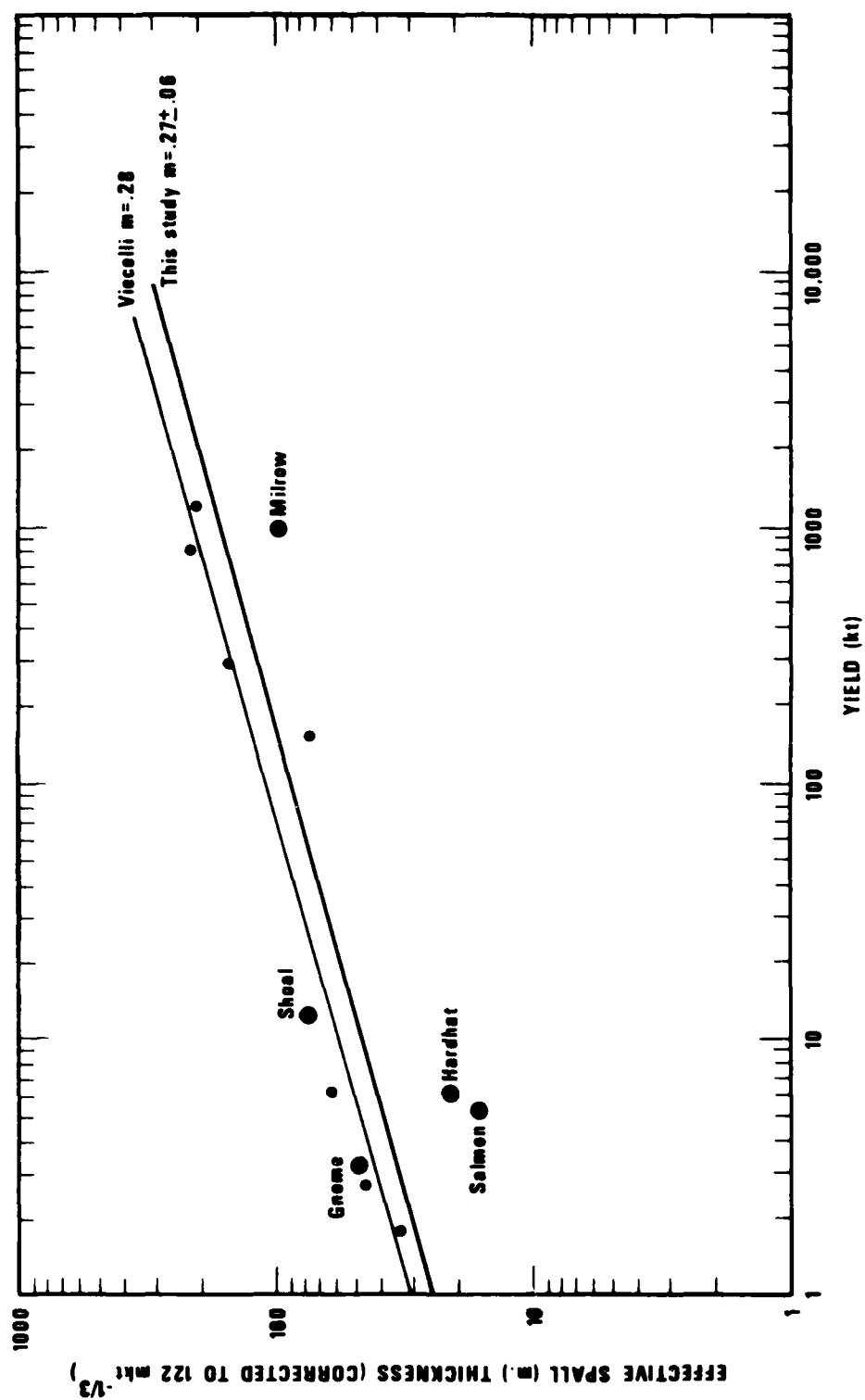
Figure 6. Effective spall thickness (corrected to 122 $mkt^{-1/3}$) vs. yield.
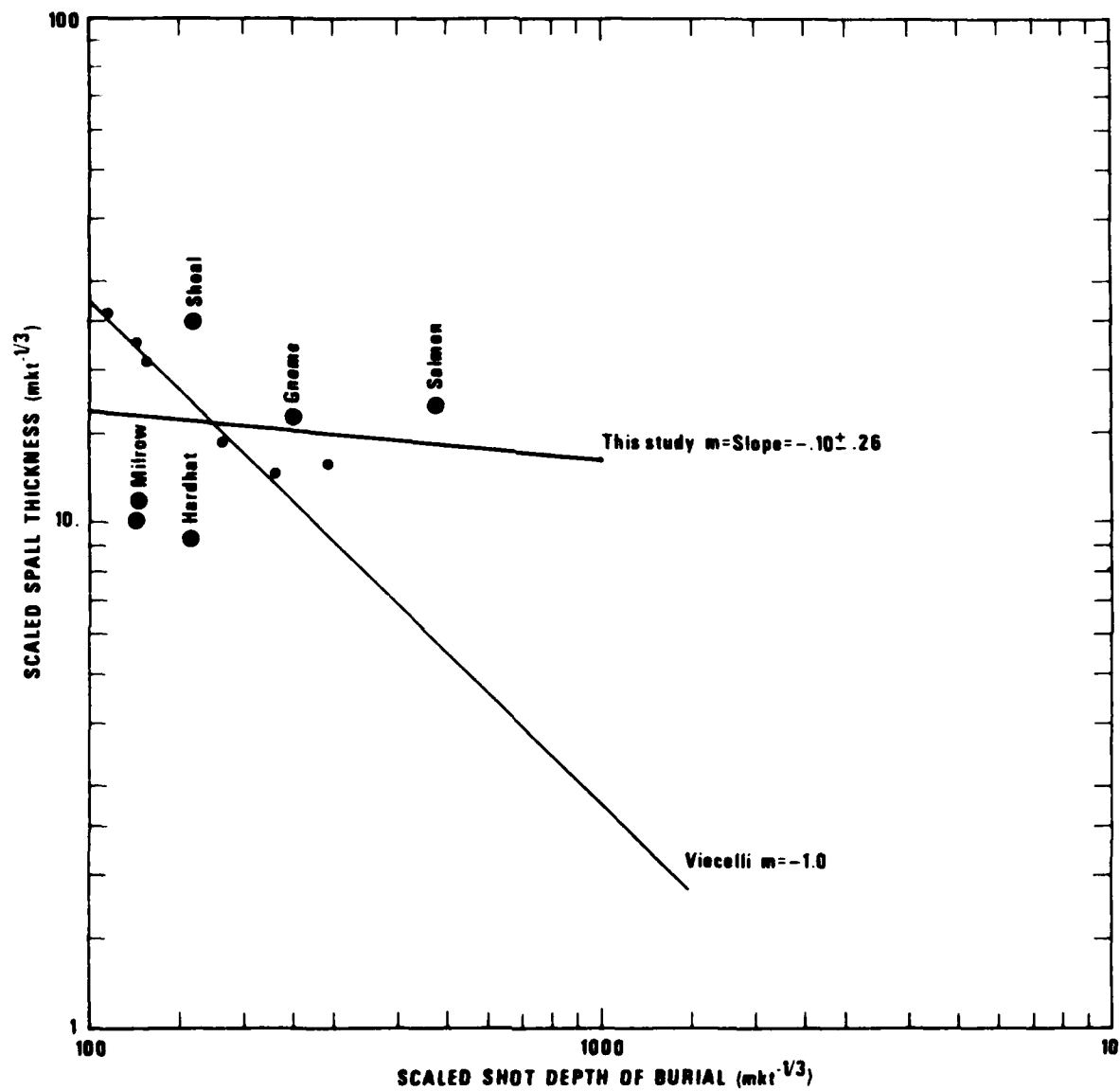
Figure 7.   Scaled   spall thickness vs. scaled shot depth of burial.
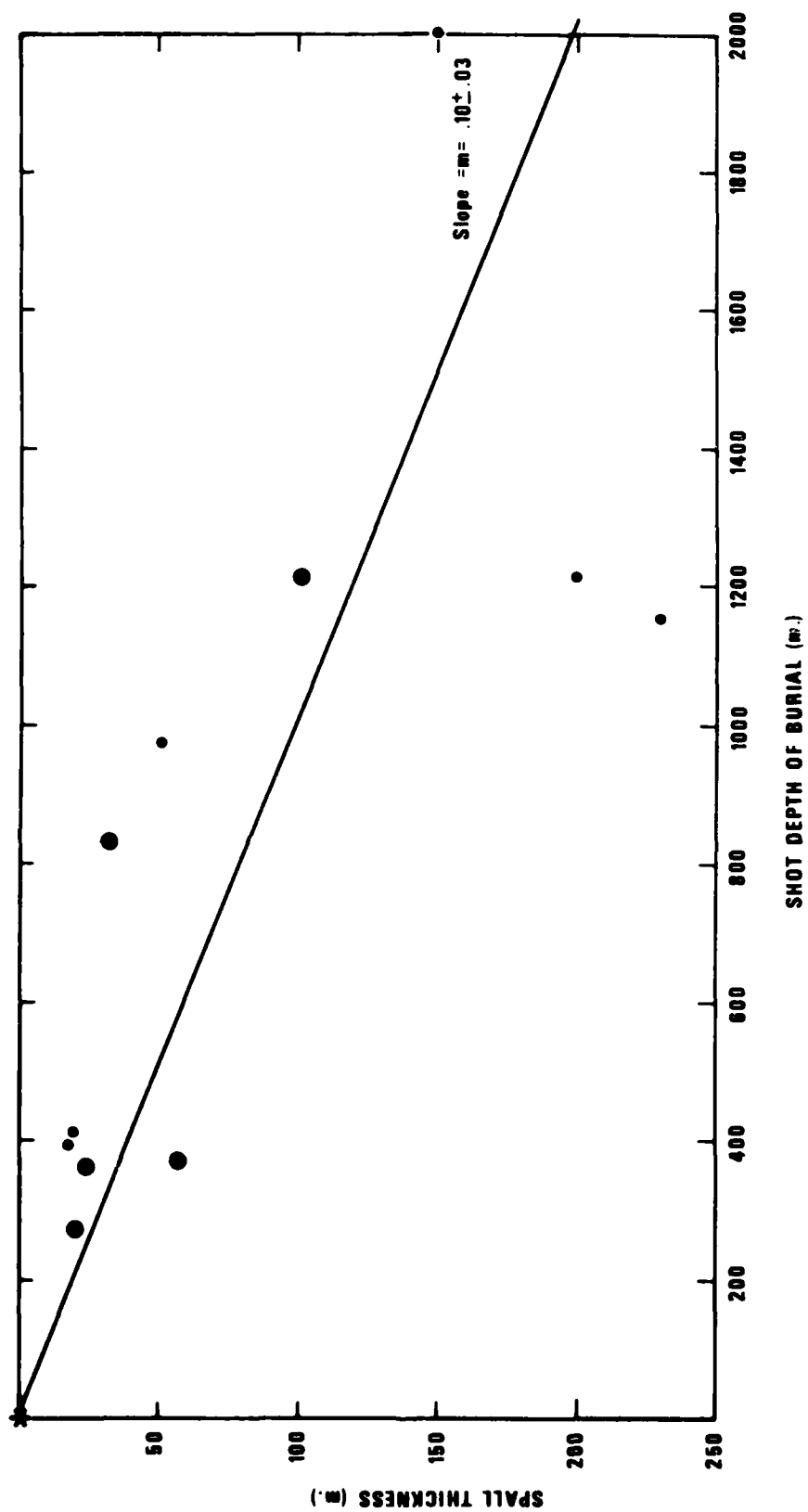
Figure 8. Spall thickness vs. shot depth of burial
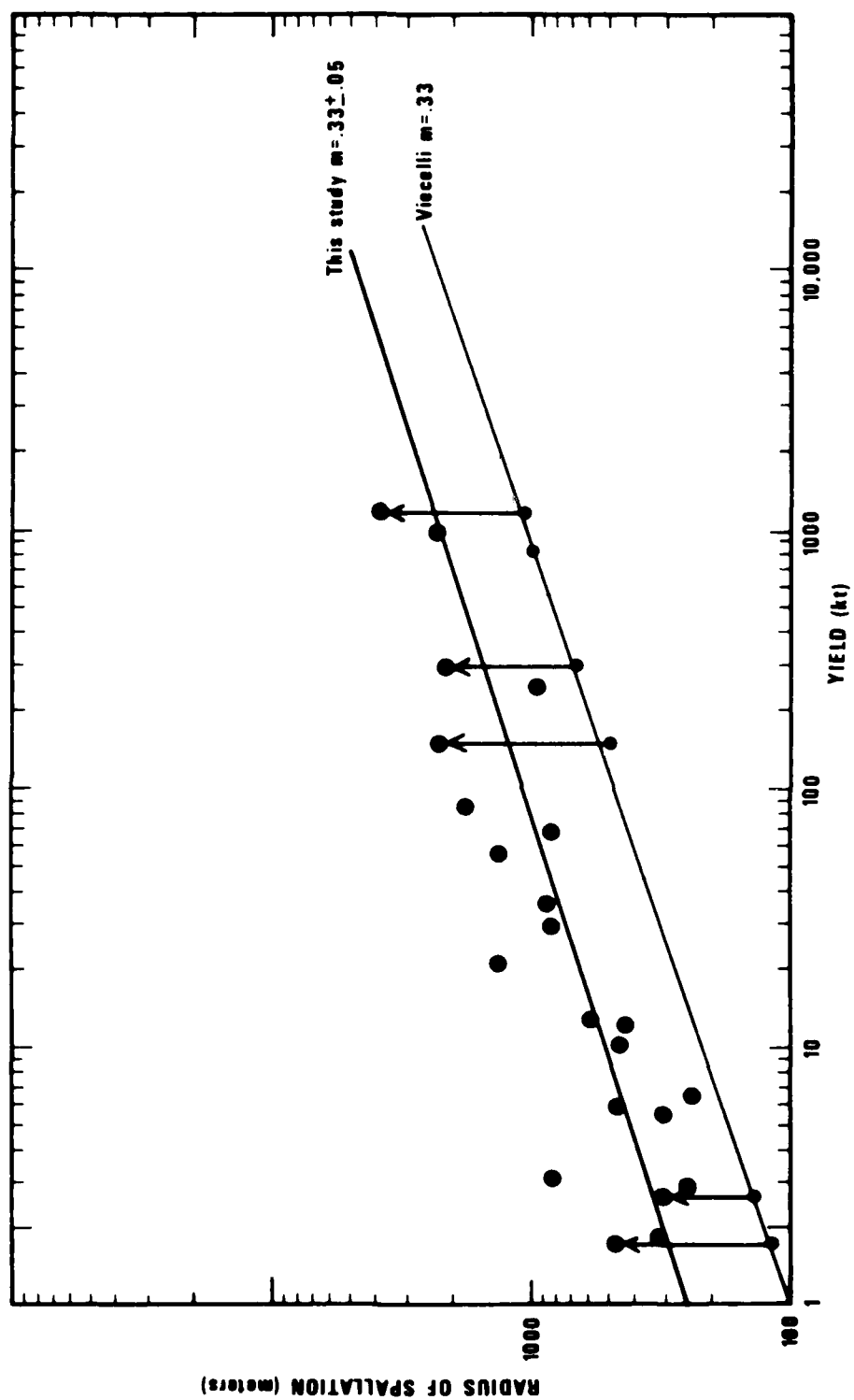
Figure 9. Radius of spallation vs. yield.
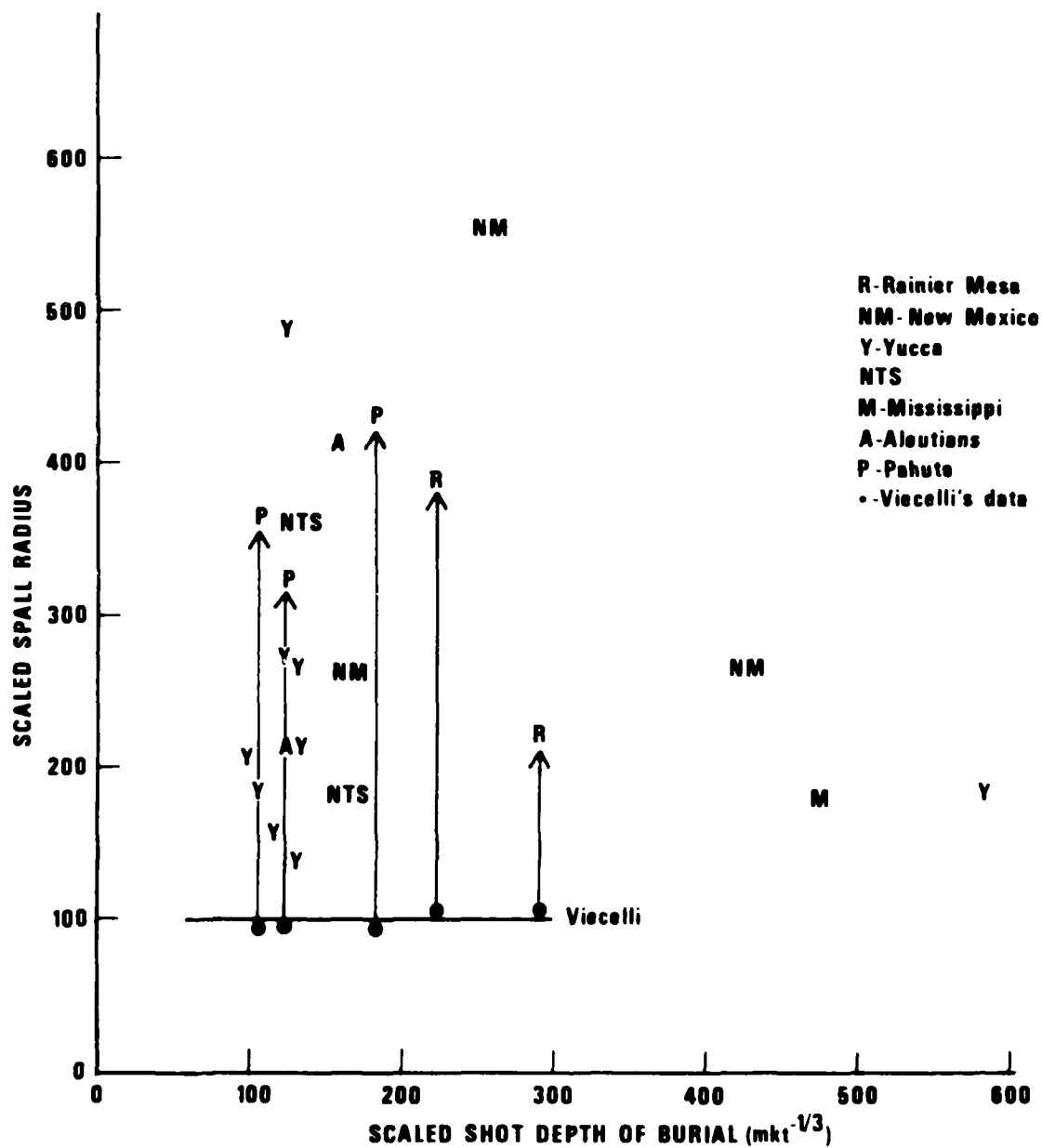
Figure 10. Scaled spall radius vs. scaled shot depth of burial.
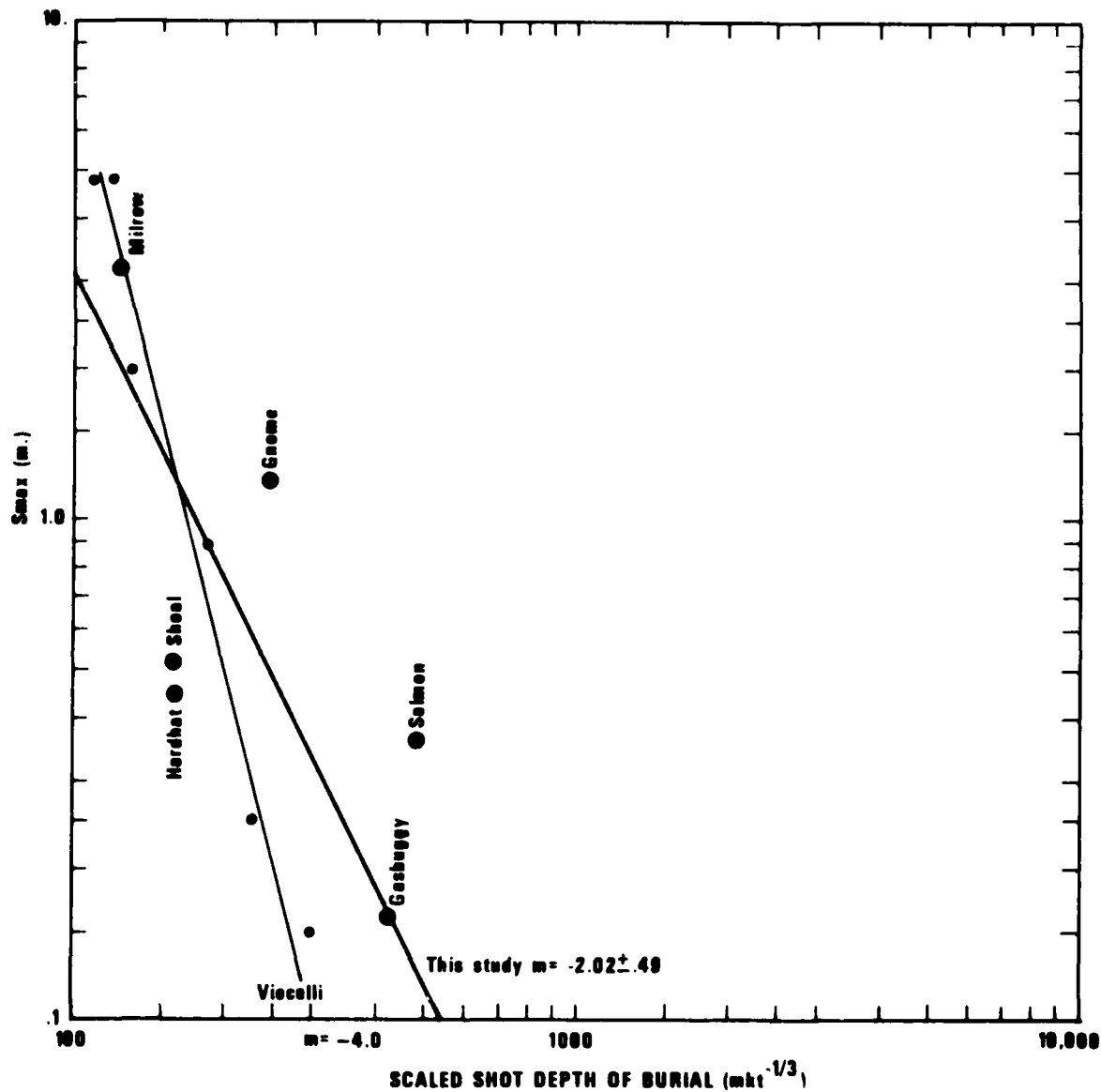
Figure 11. S_{max} (maximum height attained by spall) observed near the source vs. scaled shot depth of burial.

10.

A
A
O

5.

O

A

O

Smax (m.)

1.0
O

.5

M

m = -1.57± .49

1
100   200   1000   10.000

SCALED SHOT DEPTH OF BURIAL (mkt$^{-1/3}$)

O NTS
● NEW MEXICO
M MISSISSIPPI
A ALEUTIANS
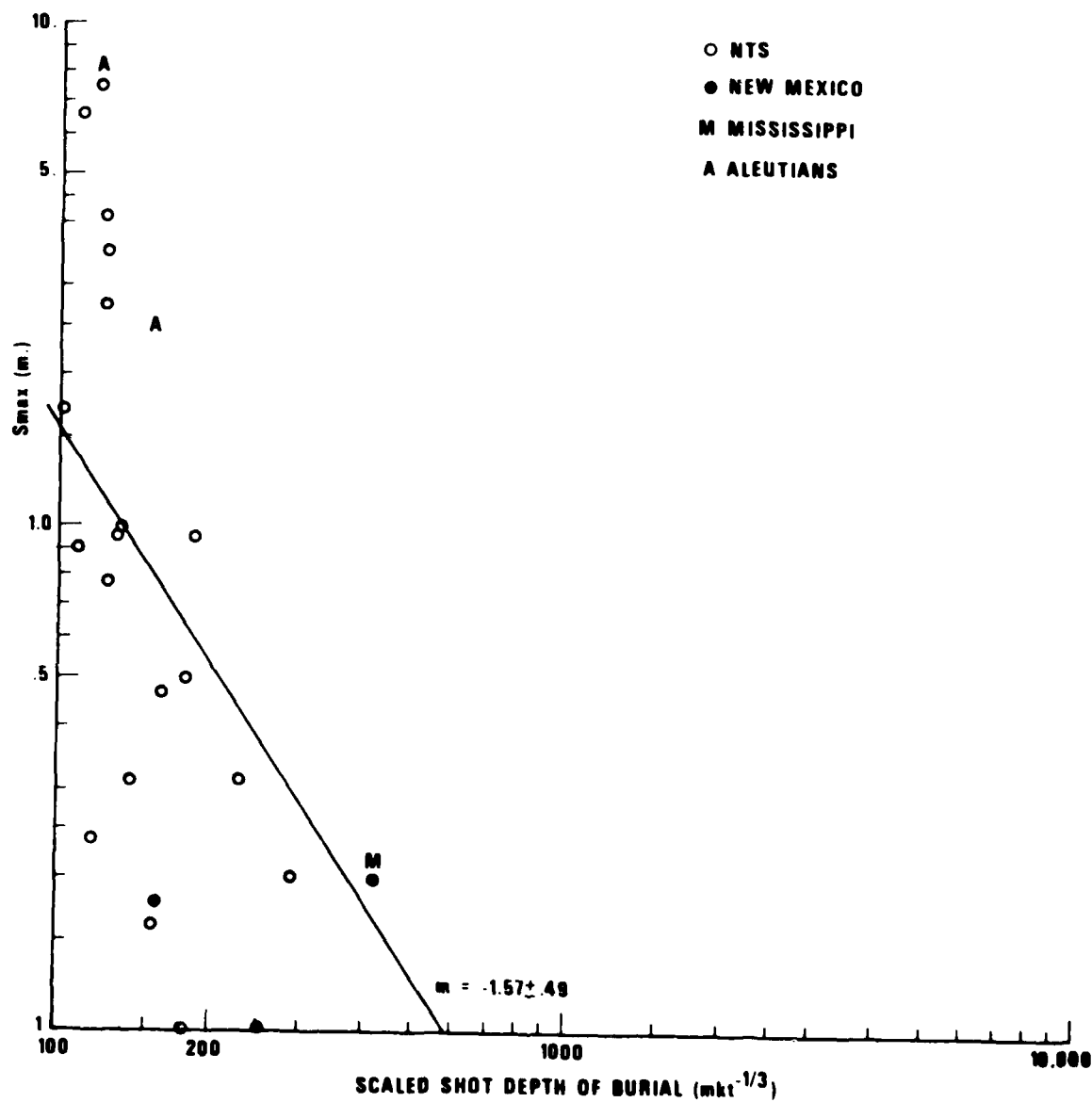
Figure 12. S_{max} calculated from $(\Lambda t)^2 g/8$ vs. scaled
shot depth of burial.   All the data points
are from this study.
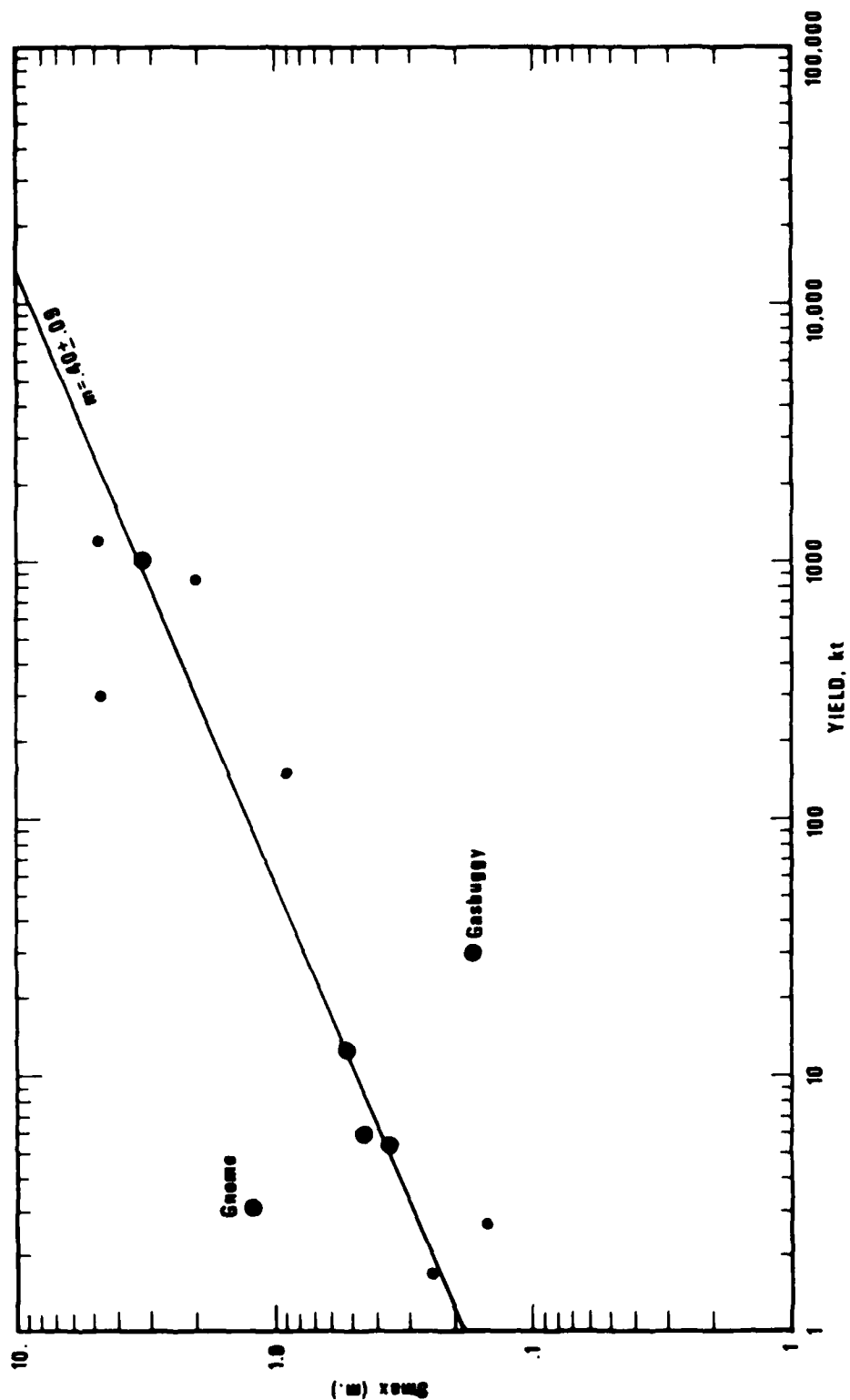
Figure 13. S_{max} observed near the source vs. yield.
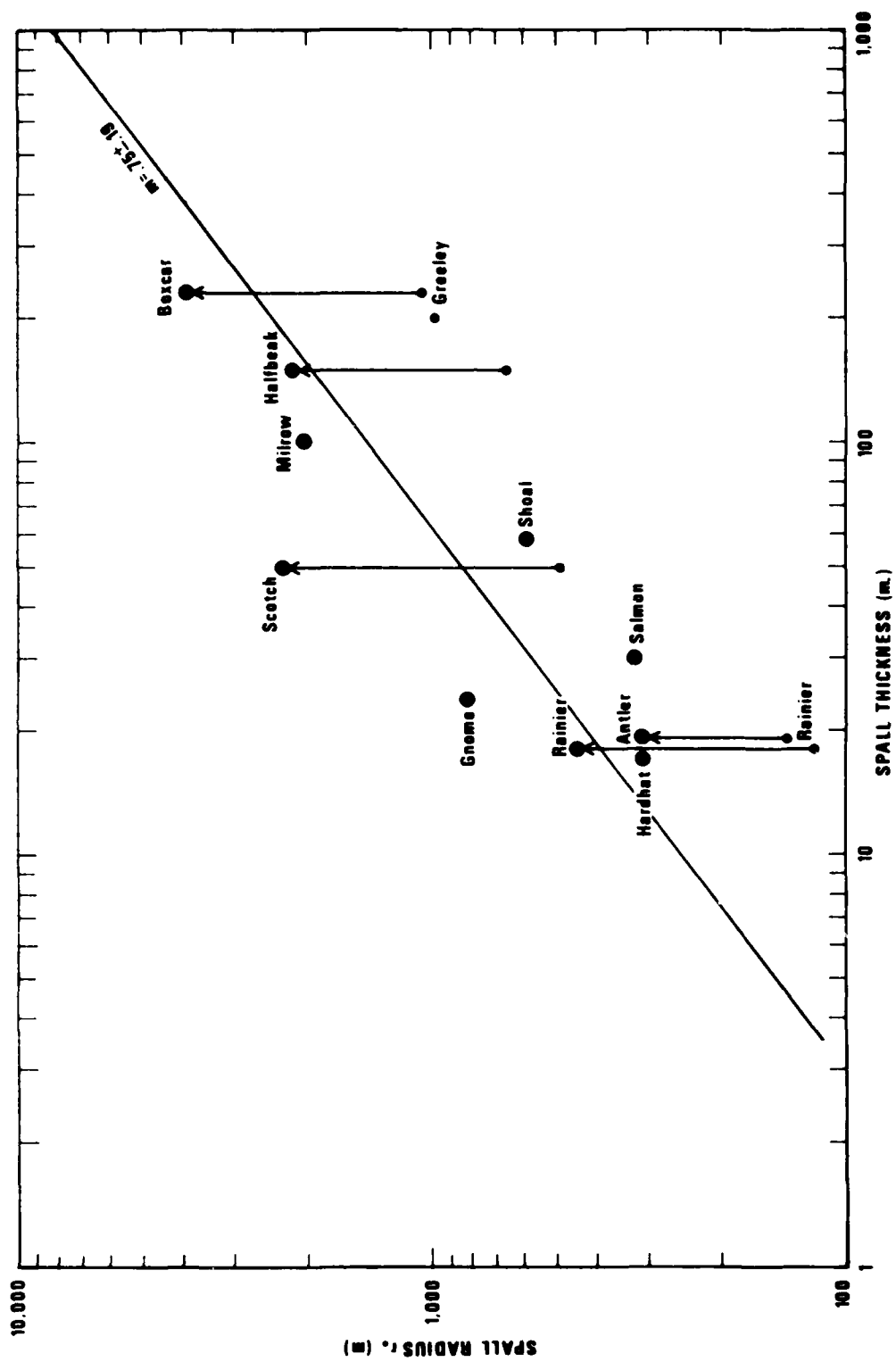
Figure 14. Spall radius vs. spall thickness.

- 28 -

TABLE I

Spall Parameters

Shot	Yield (kt)	Scaled shot depth of burial ($mkt^{-1/3}$)	Spall thickness observed (m)	Radius of spall (m)	S_{max} (m) Vertical accelerometer array	Calculated from $\dfrac{\Delta t^2 g}{8}$
RAINIER	1.7	227	18	458	.25	.31
ANTLER	2.6	292	19	301	.15	.20
FISHER	13	155				.16
GNOME	3.1	248	24	805	1.2	.10
STOAT	4.7	180				.10
ARMADILLO	6.5	129		244		.95
HARDHAT	5.9	159	17	305	.45	.47
CHINCHILLA I	1.8	123		335		.79
DORMOUSE PRIME	11	117				.24
AARDVARK	36	131		880		1.00
HAYMAKER	67	100		824		1.71
SHOAL	12.5	158	58	596	.52	.18
SALMON	5.3	475	30	320	.36	.20
HANDCAR	12	176		427		.50
MUDPACK	2.7	109		259		.91
MERLIN	10	137		457		.31
LONGSHOT	85	159		1798		2.55
DISCUS THROWER	21	122		1341		3.55
PILEDRIVER	56	121		1372		2.77
HALFBEAK	300	122	150	2134	4.8	4.07
COMMODORE	250	118		969		7.56
SCOTCH	150	184	50	2291	.9	.95
GASBUGGY	29	421		802	.17	.20
BOXCAR	1200	109	230	3813	4.8	6.62
MILROW	1000	122	100	2010	3.20	4.44
GREELEY	825	130	200		2.0	

a smaller y-intercept value. In Figure 6 the spall thickness, corrected to a scaled depth of burial of HALFBEAK (spall thickness X scaled depth of burial /122m $kt^{-1/3}$) is plotted versus yield. The adjusted data show the same scatter as in Figure 5. Figure 7 shows scaled spall thickness (thickness/ $yield^{1/3}$) versus scaled shot depth of burial (depth/$yield^{1/3}$). Viecelli found an inverse relationship between scaled spall thickness and scaled depth of burial, but the addition of new data points shows a much poorer fit to the best fit line through the entire data set. A plot of spall thickness/shot depth versus scaled shot depth of burial showed no relationship between those two variables. In Figure 8 spall thickness is plotted versus shot depth of burial. The line through the data has a slope of $.10 \pm .03$ and spall thickness is observed to range from 5 to 20 percent of shot depth.

In Figure 9 the radius of spallation is plotted versus yield. Viecelli's best fit line is a lower bound to the new set of data. A line of similar slope has been drawn through the new set of data. Both lines have a slope of 1/3, suggesting the same dependence on yield as the thickness of the spall. Figure 10 shows the scaled spall radius (radius/$yield^{1/3}$) versus the scaled shot depth of burial. No line could be found to fit the complete data set. Viecelli's seven explosions all had scaled shot depth of burial values in the limited range 95 to 105, but Viecelli's line is merely a lower bound for our data set, which contains a greater range of scaled shot depth. Great variation exists in scaled spall radius, even within a particular region.

S_{max} versus scaled shot depth of burial is shown in Figures 11 and 12. In Figure 11 S_{max} was observed near the source and in Figure 12 S_{max} was calculated from observed maximum Δt. Viecelli's data exhibits an inverse fourth power dependence on depth, but the complete set of data in this study shows an inverse second power dependence on depth and much more scatter than Viecelli's data set. In Figure 13 S_{max} observed near the source is plotted versus yield. The best-fit line has a slope of $.40 \pm .09$.

Combining the results of Figures 5 and 9, Figure 14 shows spall radius versus spall thickness. The data show a direct relationship, but the slope of a line through the data is poorly defined. Clearly, data in Figures 5 and 9 show that both spall depth and radius are dependent on yield.

- 30 -

Lateral and vertical changes in lithology probably are the major factors that affect the relationship between spall radius and spall thickness.

Possible relationships between yield (Y), shot depth (h), spall thickness (D), radial extent of spall (r_0), and maximum height the spall is thrown (S_{max}) were investigated using a multivariate general linear hypothesis program. The following relationships were found between the variables:

$$\log(D) = 1.35 + 0.35\log(Y) - 0.07\log(h)$$

$$\log(r_0) = 2.84 + 0.37\log(Y) - 0.16\log(h)$$

$$\log(S_{max}) = 0.57 + 0.52\log(Y) - 0.50\log(h)$$

The effect of shot depth is significantly different from zero only at the 50 percent level, implying that shot depth is not a significant variable. Shot depth probably is a significant variable but this cannot be shown because of the strong correlation of depth with yield and the small number of observations (12 cases). Both $\log(D)$ and $\log(r_0)$ are approximately proportional to (1/3) $\log(Y)$, as seen in Figures 5 and 9.

ESTIMATES OF TELESEISMIC pP AND P_{SPALL} ARRIVAL TIMES
FROM NEAR-FIELD DATA

Springer (1974) estimated P_{SPALL}-P times for explosions at teleseismic distances using near-field surface accelerometer data that show t_{up}, the uphole travel-time above the source, and Δt, the difference between the spall arrival time and the direct ray. Springer assumed that the spall signal on the surface accelerometer data is due to the first, and deepest, spall closure. Δt is a function of distance from the source and it is generally largest over the source where the free-fall time of spall is largest. (Figures 2 and 3). pP-P at teleseismic distances can be approximated by the formula

$$pP-P = 2t_{up}\cos\theta$$

where θ is the take-off angle at the source. P_{SPALL}-P can be approximated by the formula

$$P_{SPALL}-P = \Delta t + \frac{2t_{up}}{\cos\theta} - .2t_{up}$$

(Springer 1974). Where no information on spall depth is available, the travel-time between the spall depth and the surface is assumed to be 20 percent of the uphole time, which accounts for the term $.2t_{up}$.

Table II lists pP-P and P_{SPALL}-P times for 47 explosions. pP-P times are from already published values of t_{up}. An epicentral distance of 50 degrees was used in the calculations. P_{SPALL}-P times are from published near-field surface accelerometer measurements, particle velocity tables of near-field data provided by Sandia Laboratories, and Springer's (1974) study. The Δt values that Springer used were near the shot hole, where energy was assumed to be at a maximum. Since this is also the maximum value of Δt found, Springer's P_{SPALL}-P times are maximum values. As demonstrated in the next section, the velocity of the slab at impact and, therefore, the relative energy of spallation varies with distance from the shot hole. The impact of the disc occurs over a time range of a few tenths of a second for most explosions and the maximum energy as a function of radius occurs near

---

Springer, D., 1974. Secondary sources of seismic waves from underground nuclear explosions, Bull. Seism. Soc. Amer., 64, 581.

TABLE II

Teleseismic pP-P and P_{SPALL}-P Estimates.

Shot	Date	Location °N	°W	Yield (kt)	Depth of Burial (m)	pP-P(sec)	P_{SPALL}-P (sec) Acceler-ometers	Particle Velocities	Springer
RAINIER	09-19-57	37	116	1.7	274	.27		.57	.75
ANTLER	09-15-61	37	116	2.6	402	.27		.57	
SHREW	09-16-61	37	116	0-20	98	.11		.26	
MINK	10-29-61	37	116	0-20	192	.22		.46	
FISHER	12-03-61	37	116	13	364	.36		.75	
GNOME	12-10-61	32	104	3.1	362	.29	.61	.56	1.32
RINGTAIL	12-17-61	37	116	0-20	363	.36		.67	
STOAT	01-09-62	37	116	4.7	302	.33		.64	
DORMOUSE	01-30-62	37	116	0-20	363	.36		1.13	
ARMADILLO	02-09-62	37	116	6.5	240	.29		1.20	
HARDHAT	02-15-62	37	116	5.9	287	.12		.44	
CHINCHILLA I	02-19-62	37	116	1.8	150	.17		.51	
PLATYPUS	02-24-62	37	116	0-20	58	.07		.15	
PAMPAS	03-01-62	37	116	0-20	363	.36		.79	
ERMINE	03-06-62	37	116	0-20	73	.08		.15	
HOGNOSE	03-15-62	37	116	0-20	239	.28		.95	
CHINCILLA II	03-31-62	37	116	0-20	137	.16		.81	
DORMOUSE PRIME	04-05-62	37	116	11	261	.29		.76	
AARDVARK	05-12-62	37	116	36	434	.27		.80	
RACCOON	06-01-62	37	116	0-20	164	.19		.47	
PACKRAT	06-06-62	37	116	0-20	262	.29		1.02	
DAMAN I	06-21-62	37	116	0-20	260	.29		.72	
HAYMAKER	06-27-62	37	116	67	408	.40		.86	
CLEARWATER	10-16-63	37	116	200-1000	544	.46		.96	
SHOAL	10-26-63	39	118	12.5	367	.17	.61	.56	.90
SALMON	10-22-64	31	90	5.3	828	.47	.86	.86	
HANDCAR	11-05-64	37	116	12	402	.30		.85	.92
MUDPACK	12-16-64	37	116	2.7	152	.10		.83	
MERLIN	02-16-65	37	116	10	296	.11	.49	.52	
DILUTED WATERS	06-16-65	37	116	0-20	195	.23		1.06	
LONGSHOT	10-29-65	51	179E	85	701	.37		1.34	1.76
PINSTRIPE	04-25-66	37	116	0-20	296	.35		1.04	
DISCUS THROWER	05-27-66	37	116	21	337	.33		2.06	
PILEDRIVER	06-02-66	37	116	∿56	463	.19		1.71	1.32
HALFBEAK	06-30-66	37	116	300	820	.58		1.44	2.93
NEW POINT	12-13-66	37	116	0-20	244	.28		1.05	
AGILE	02-23-67	37	116	20-200	732	.67		1.38	
COMMODORE	05-20-67	37	116	250	746	.68		2.50	
SCOTCH	05-23-67	37	116	150	977	.75		1.44	1.73
DOORMIST	08-31-67	37	116	0-20	446	.27		.66	
LANPHER	10-18-67	37	116	20-200	714	.71		2.17	
GASBUGGY	12-10-67	37	107	29	1292	.71	1.02	1.02	1.17
FAULTLESS	01-19-68	39	116	200-1000	975	.66		1.26	2.17
KNOX	02-21-68	37	116	20-200	645	.55		1.30	2.47
BOXCAR	04-26-68	37	116	1200	1158	.79		3.18	3.07
CYPRESS	02-12-69	37	116	0-20	411	.27		.60	
MILROW	10-02-69	51	179E	∿1000	1219	.61	1.26	1.30	2.49

the shot hole, but generally not at the accelerometer closest to the shot hole. For each explosion, the impact energy was calculated at each accelerometer site for an annulus of 1 cm width and a thickness equal to the spall thickness. Where the energy was highest the value of Δt at that accelerometer was used in the calculation of teleseismic $P_{SPALL}-P$. Because the source of the P_{SPALL} signal extends over a fraction of a second or more, most workers thought that identification of the signal depended upon the arrival time of the maximum energy and not the arrival time of the earliest energy, which may be too small to be observed at teleseismic distances. Note that over half of the $P_{SPALL}-P$ times are approximately one second or less. The separation times between P, pP and P_{SPALL} may be too small in these cases to be resolved by conventional techniques. Since the deeper events would have greater times of separation between P, pP, and P_{SPALL}, the best chances for detection of pP and P_{SPALL} are for the deeper events (depth of burial greater than 500 m at NTS).

SPALL ENERGY AND ITS EFFECTS ON m_b AND M_s

Energy (ergs) as a function of range was calculated for all explo-
sions using the formula

ENERGY(r) = $2\pi r D \Delta r \delta 2gh(r)$

where r is the horizontal range, D is the spall thickness, δ is the over-
burden density, g is gravitational acceleration, and $h(r)$ is the height to
which the spall is thrown. For each explosion the impact of an annulus of
one cm diameter (Δr equals one cm) was calculated at each accelerometer site.
Figure 15 shows estimated energy as a function of range for five explosions.
These five explosions, shown in a later section, have relatively high
spall energy compared to the energy of the explosion. No relationship
exists between the range of maximum energy and spall thickness, spall
radius, or geographic location. However, there was direct relationship
between yield and the range of maximum spall energy (Figure 16).
For the entire set of 47 explosions, the radius of maximum spall energy
ranged from 9 to 100 percent of the maximum radius of spall.

Figure 17 shows the energy values shown in Figure 15 plotted as a
function of time after the origin time of the explosion. Each vertical line
represents the energy of impact at the radius of an accelerometer site for an
annulus of one cm diameter. The data has been sampled discontinuously at each
of the near-field accelerometer sites and the dashed lines between energy
measurements suggest continuous production of energy as the slab impacts
over a time interval of less than a second for these five explosions. The
teleseismic spall signal would be emergent with smaller energies from
the closures at large distances from the shot hole that arrive before the
higher energies from closures at closer distances to the shot hole where
free-fall time is greatest.

The author wanted to examine the relative energy of spallation compared
to the explosion's energy. From a knowledge of the mass of the falling slab
and the height to which it is thrown, the total energy in a falling slab can
be calculated. Tables that Sandia Laboratories provided gave the height the
slab was thrown as h_i at distance r_i. The slab is divided into annuli
centered about the explosion. The radii from the explosion to the outer
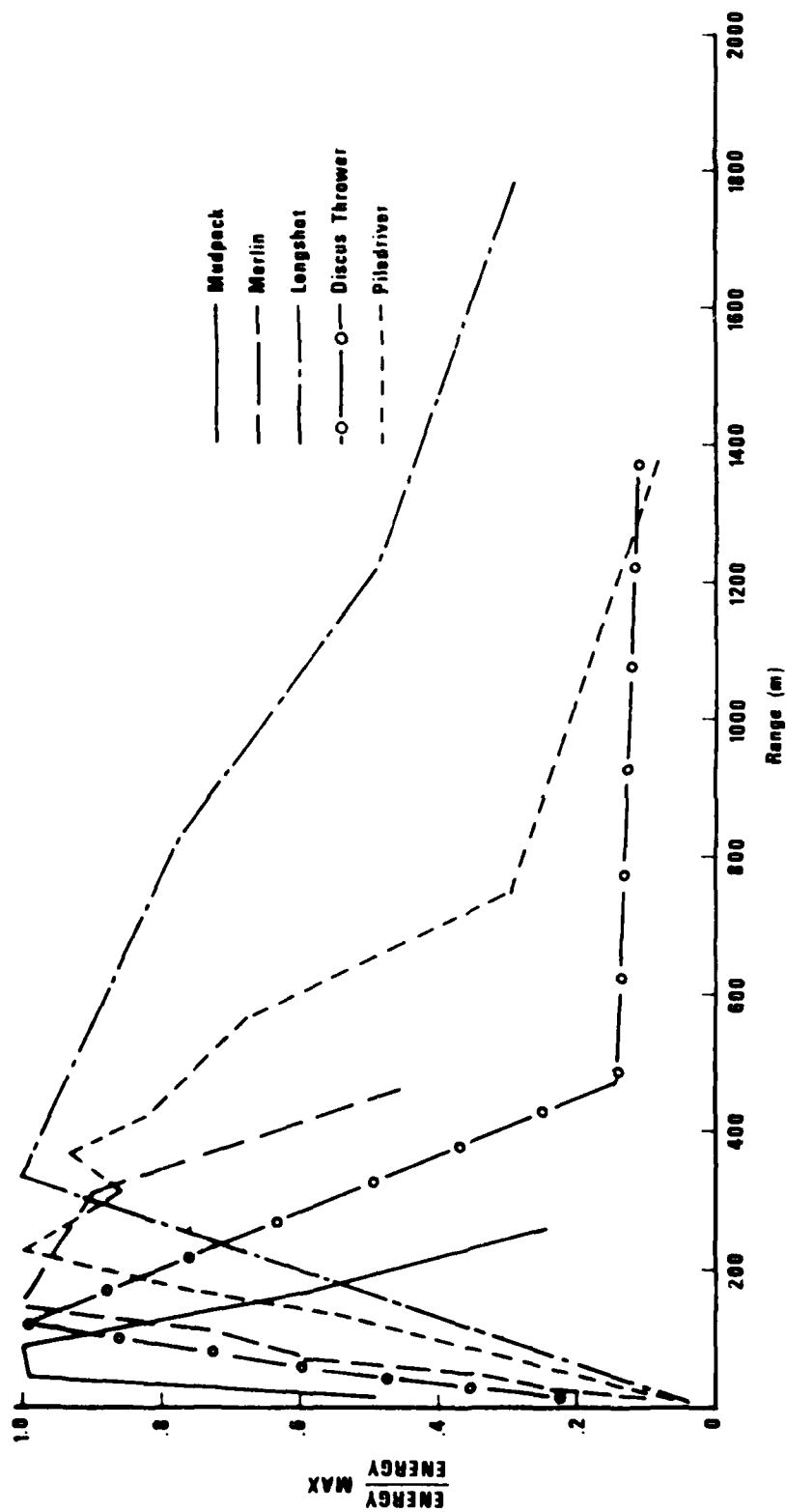
Figure 15. Energy vs. range for five spall closures.
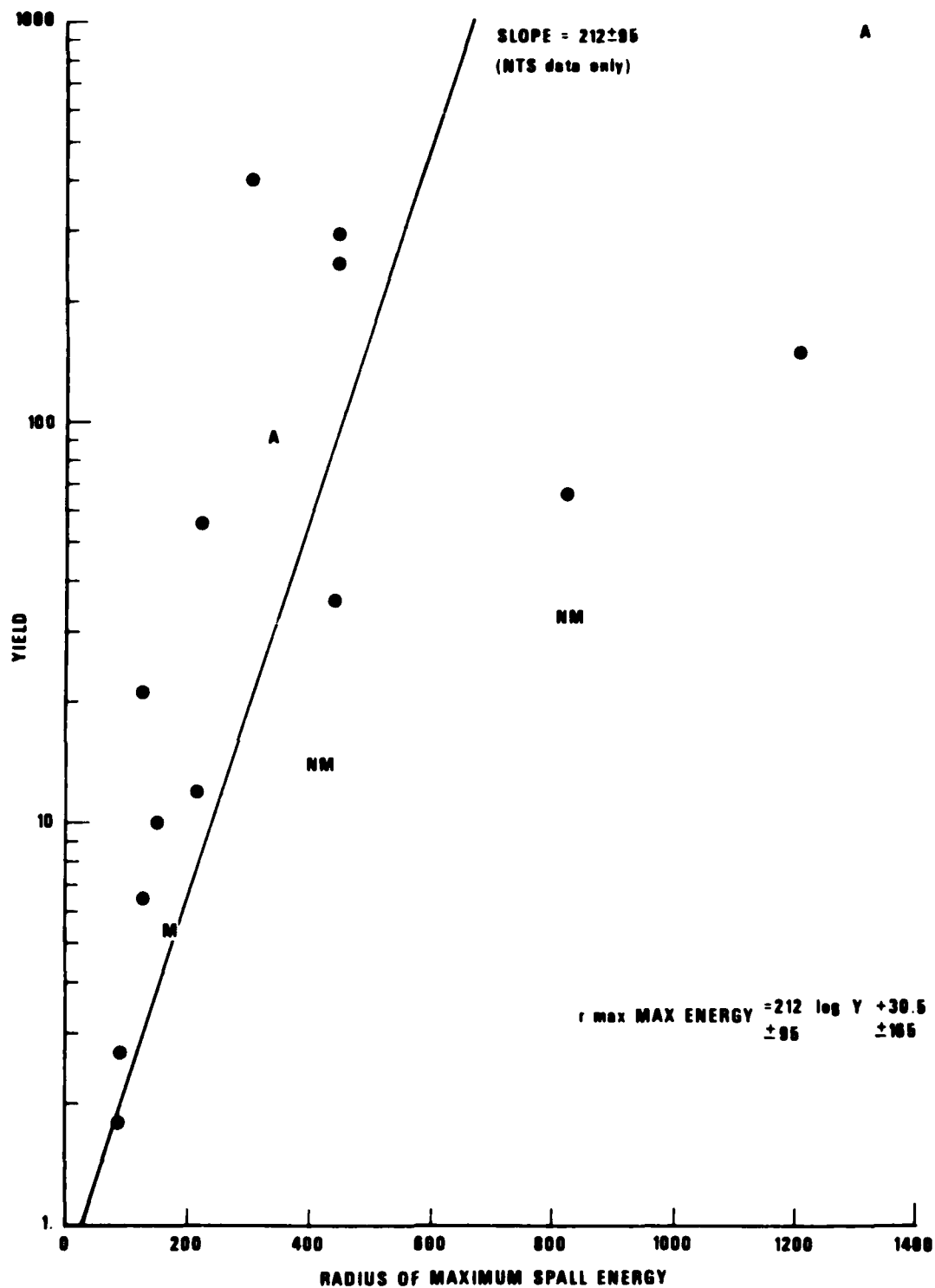
Figure 16. Yield vs. radius of maximum spall energy.
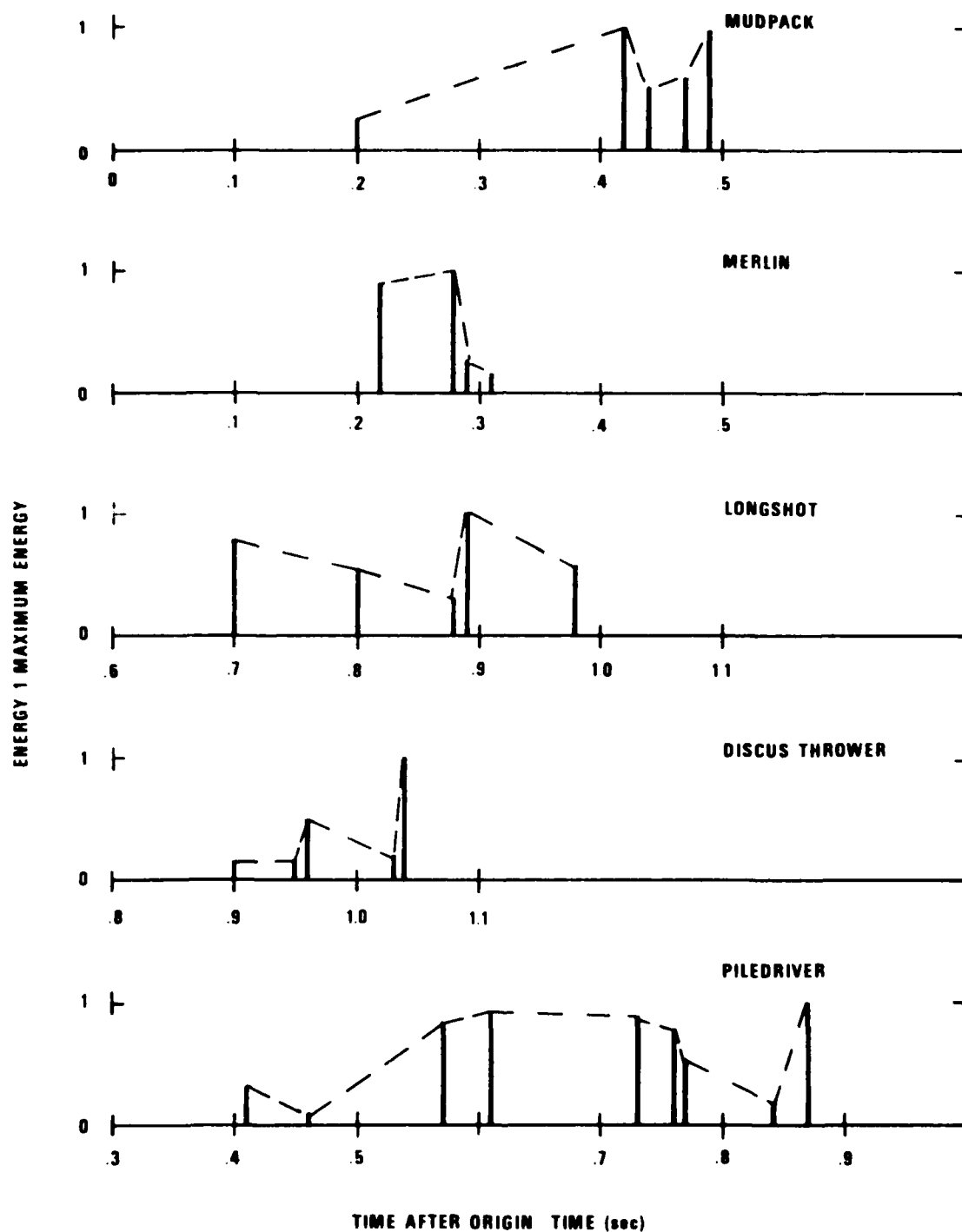
Figure 17. Energy vs. time for spall closure.

and inner boundaries of the annuli would be the radii where the height
of the thrown slab was measured. By summing the individual contributions
from each falling annulus the total energy would be found

$$\text{ENERGY (ergs)} = \sum_{i=1}^{N} 2\pi r_i D \Delta r_i \delta V_0^2$$

where N = number of annuli or number of observation sites

r_i = the distance to the center of each annulus,

$$r_i = \frac{R_i + R_{i-1}}{2}$$

D = thickness of annuli (spall thickness)

Δr_i = width of annuli, $r_i = R_i - R_{i-1}$

δ = density of annuli

V_0 = velocity of slab at impact,

$$V_0^2 = 2gh(r) \text{ and } h(r) = \frac{H_i + H_{i+1}}{2}$$

If the spall thickness was not available from vertical accelerometer arrays,
or observed parting in the boreholes, then spall thickness was assumed to be
10 percent of the shot burial depth, a figure suggested by the relationship
between spall thickness and shot depth of burial in Figure 8. Table
III shows the spall and explosion energies for the explosions with known
yields. Explosion energies were found in Perret (1972) or were calculated
with the efficiencies for various mediums found in Perret's study according
to the formula

$$\text{ENERGY (ergs)} = \text{Yield(kt)} \times \text{Efficiency} \times 4.18 \times 10^{19} \qquad (1)$$

To examine the amount of energy that spall generated compared to the energy
of the explosion, the ratio of these two values for each explosion was plotted
versus yield (Figure 18). The explosion had spall energies that were from 1 to
322 percent of the explosion energies. Obviously, errors exist in the assump-
tions used to calculate the spall energy or the radiated energy since the spall
energy cannot exceed that fraction of the explosion energy traveling upward into

Perret, W., 1972. Seismic-source energies of underground nuclear explosions,
    Bull. Seism. Soc. Amer., 62, 763.

TABLE III.

Spall Energies

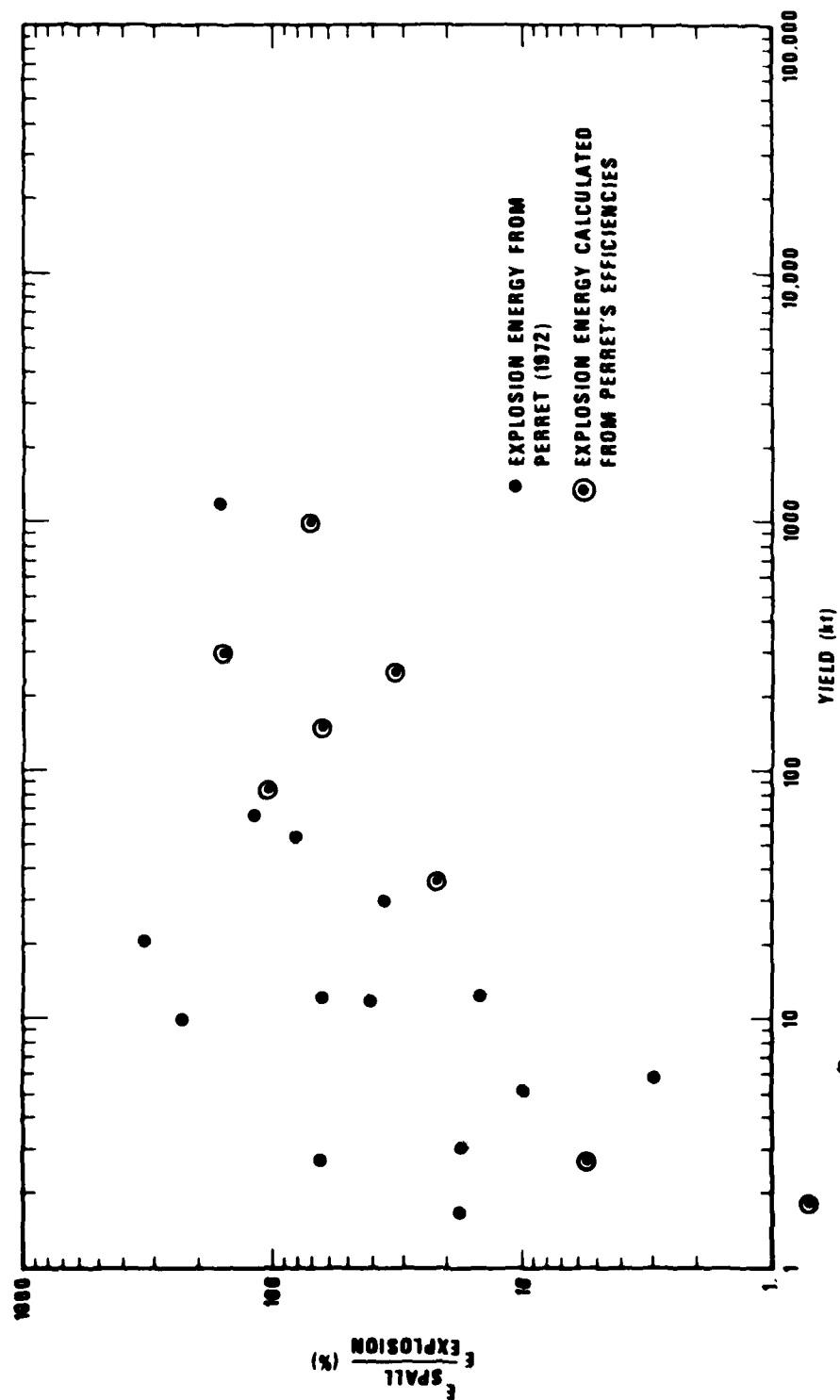| Explosion	Spall Energy (10^{19} ergs)	Explosion Energy (10^{18} ergs)		$\dfrac{E_{SPALL}}{E_{EXPLOSION}}$	M_s (von Seggern)
		Perret	Calculated*		
RAINIER	.027	1.5		.18	
ANTLER	.012		2.2	.06	
FISHER	.002	.68		.03	
GNOME	.214	12.		.18	
ARMADILLO	.0135		27.2	.01	
HARDHAT	.0245	8.4		.03	3.01
CHINCHILLA I	.0056		7.5	.01	
AARDVARK	.666		30.1	.22	3.56
HAYMAKER	.324	2.7		1.20	3.02
SHOAL	.841	13.		.65	
SALMON	.075	7.6		.10	
HANDCAR	.444	11.		.40	3.03
MUDPACK	.008	.12		.66	1.76
MERLIN	.040	.17		2.36	
LONGSHOT	7.77		71.	1.09	
DISCUS THROWER	.836	2.6		3.22	3.05
PILEDRIVER	3.79	47.		.81	4.05
HALFBEAK	41.1		251.	1.64	5.06
COMMODORE	7.01		209.	.34	4.59
SCOTCH	8.00		125.	.64	4.51
GASBUGGY	.850	24.		.35	
BOXCAR	226.	1400.		1.61	5.56
MILROW	54.9		836.	.72	5.0

* Energy = Yield x Efficiency x 4.18×10^{19}

Figure 18. Spall energy /explosion energy vs. yield.

the spall region. Assuming a spherical explosion source, the fraction of
the explosion energy reaching the spall region depends upon the depth of
burial and the spall radius. For explosions studied here that fraction
ranged from 1 to 37 percent.

Spall energy was calculated for 42 NTS explosions located below the
water table that lacked near-field data. Thickness of the spall layer was
estimated from the relationship between yield and spall thickness
found in Figure 5. Similarly, the maximum radius of spall was found from
Figure 9 and the maximum height attained by spall was found from Figure 11.
The height spall was thrown was assumed to vary inversely as the square of
the horizontal distance from the shot hole, which approximates the conical
shape of spall height observed by other investigators (Figure 31). Figure
14 shows the M_s residual (M_s - log yield + constant) for these explosions
(von Seggern and Gurski, 1976) versus spall energy/explosion energy.
No relationship exists between M_s residual and spall energy/explosion energy,
a situation suggesting that spall has no effect on M_s. In addition, low
strain release events (Massé, unpublished data) do not show a clearer
relationship than do average strain release events, suggesting that strain
release is not hiding the effect of spall energy.

The efficiency that Perret (1972) calculated is a source of error
in the energy calculations. Table IV shows the explosion energies that
Perret derived from near-field data and the explosion energies calculated
for the same explosions using formula (1). The range of variation between
the two energy values for each explosion, and hence the error in estimating
explosion energies using Perret's efficiencies, ranged from a factor of 1.0
to 2.7.

Another source of error in the energy calculations is the thickness of
the spall layer. In a few cases partings were observed in boreholes. However,
there were several spall partings and the one responsible for the spall signal
on the near-field surface accelerometer data must be determined. Because most

---

von Seggern, D., and J. Gurski, 1976. M_s versus yield of underground nuclear
    explosions at the Nevada Test Sites, SDAC-TR-76-11, Teledyne Geotech,
    Alexandria, Virginia 22314.
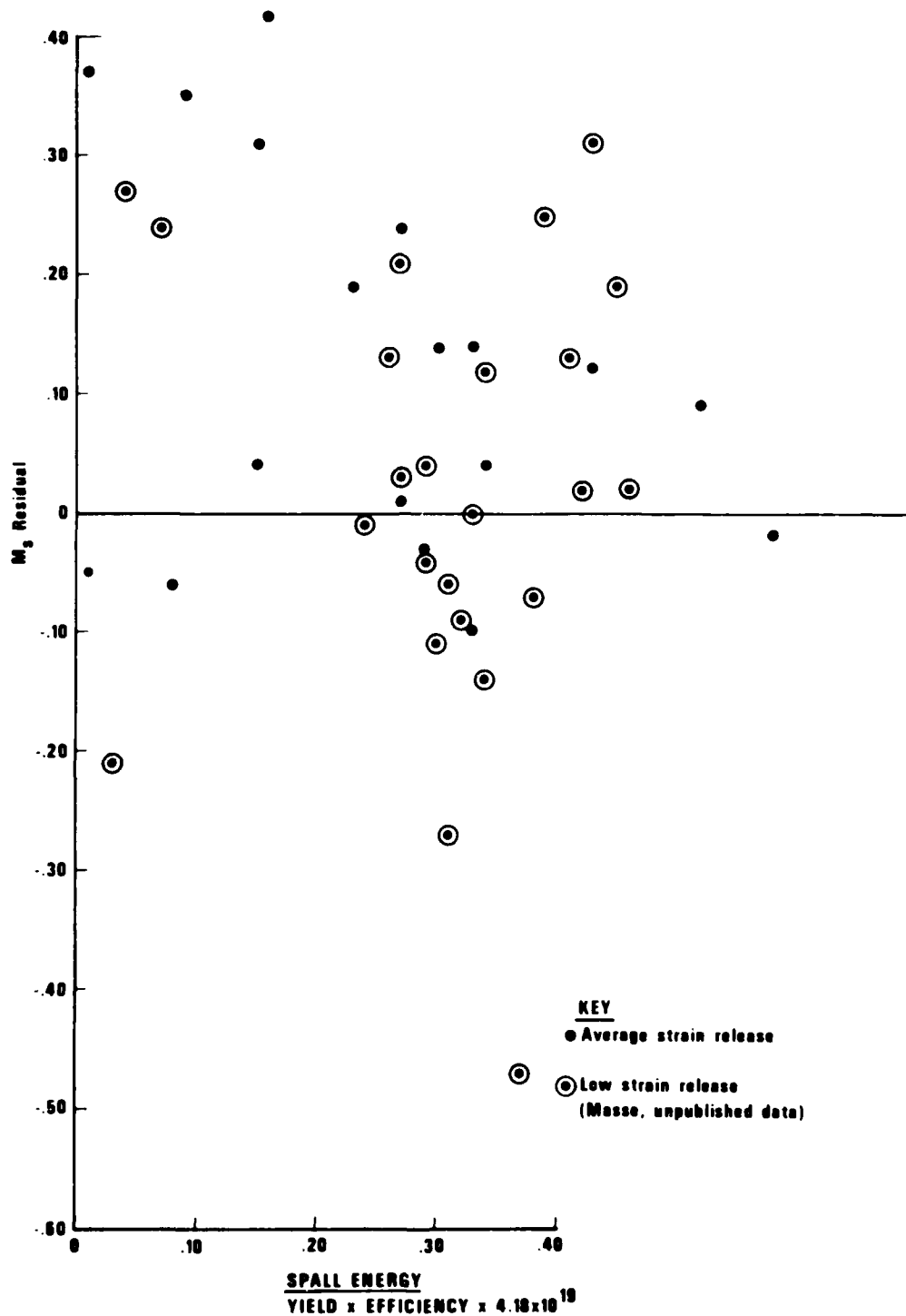
Figure 19. M_s residual vs. spall energy/explosion energy for 42 NTS explosions located below the water table.

TABLE IV.

Explosion energies from Perret (1972) and from
Perret's efficiency estimates for the explosion medium.

| Shot | Energy (10^{18} ergs) | | Differ- | | |
	Perret	Yield x efficiency x 41.8	erence (%)	Yield	Efficiency (%)
RAINIER	1.5	1.4 - 2.1	0-40	1.7	2 - 3
FISHER	.68	.27 - .82	0-60	13	.05 - .15
GNOME	12.	3.9	68	3.1	3
HARDHAT	8.4	4.9	42	5.9	2
HAYMAKER	2.7	1.40 - 4.2	0-56	67	.05 - .15
SHOAL	13.	10.4	20	12.5	2
SALMON	7.6	6.6	13	5.3	3
HANDCAR	11.	10.0	9	12	2
MUDPACK	.12	.11 - .34	0-183	2.7	.10 - .30
MERLIN	.17	.21 - .63	24-271	10	.05 - .15
DISCUS THROWER	2.6	.88 - 2.6	0-66	21	.10 · .30
PILEDRIVER	47.	47.	0	56	2
GASBUGGY	24.	24.	0	29	2
BOXCAR	1400.	1003.	28	1200	2

subsurface displacements are attributed to parting at one depth, the energy for the falling disc varies directly with the thickness of the falling disc.

In some cases spall depth was determined from observations of the arrival times of the phase t_2 and the phase reflected off the spall layer t_3. Figure 2 illustrates the ray paths of these two phases. This method of determining spall depth is suspect because identification of the presumed t_3 arrival is uncertain. If the sources of the spall signals were close to the surface, then the t_3 arrival could not be separated from the t_2 arrival, and the total amount of energy in such a thin falling disc would be small compared to the explosion energy.

In cases where subsurface vertical accelerometer arrays were used to determine spall depth, the spall depth was located between two sensor depths with the spall signal showing moveout in time above the presumed spall depth. Figures 20 through 23 show examples of near-field subsurface vertical accelerometer array data. In each case note the arrival of the initial acceleration pulse, travelling upward at the compressional velocity of the medium. Dashed lines indicate expected return of the reflected phase pP. In all cases there is little pP energy leaving the source region compared to the initial signal, suggesting that for these explosions pP is of small amplitude compared to P at teleseismic distances. Note that pP has travelled farther than P and is, therefore, expected to be smaller because of spherical divergence. The next large arrival following the initial pulse is the spall signal. GNOME and SLAMON show several spall signals. For RAINIER, assuming that all spall occurs above these depths, the data (Figure 20) shows no large spall pulses at 137-, 160- and 162- meter gauges. Similarly, spall is assumed to occur above 91 meters for SALMON (Figure 22) and above 1000 feet for MILROW (Figure 23). Spall closure signals in Figures 20 through 23 propagate upward at a speed slower than the compression velocity of the medium. Thus, spalling is presumed to occur over a range of depths. Deeper formations close before shallower layers and accelerometer data show each spall phase occurs in the first cycle caused by the spall closure closest to that gauge. The total energy in spall closure probably results from summing at least several spall closures and not from initial spall impact.
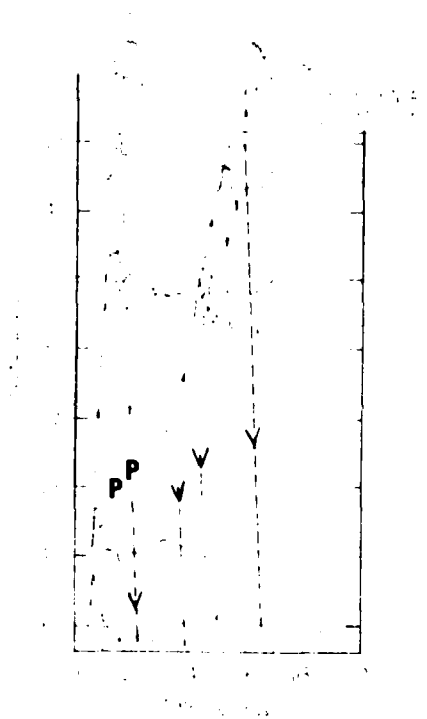
Figure 20. Subsurface vertical accelerometer array data
for RAINIER (Eisler, Chilton, and Sauer, 1966).
Arrows indicate the direction of flow of seismic
energy.
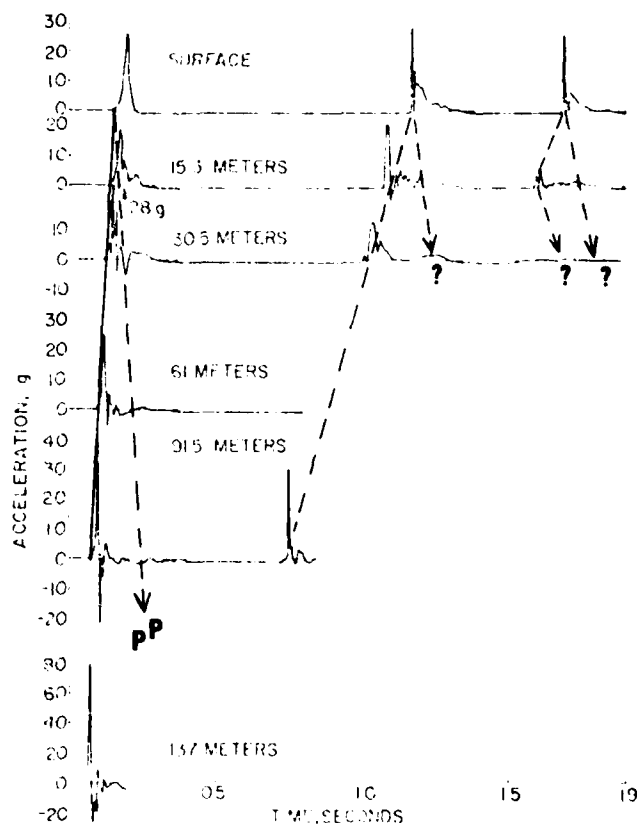
Figure 21. Subsurface vertical accelerometer array data
for GNOME (Weart, 1962). Lower gauges suffer
from early cable failure. Arrows indicate the
direction of flow of seismic energy.
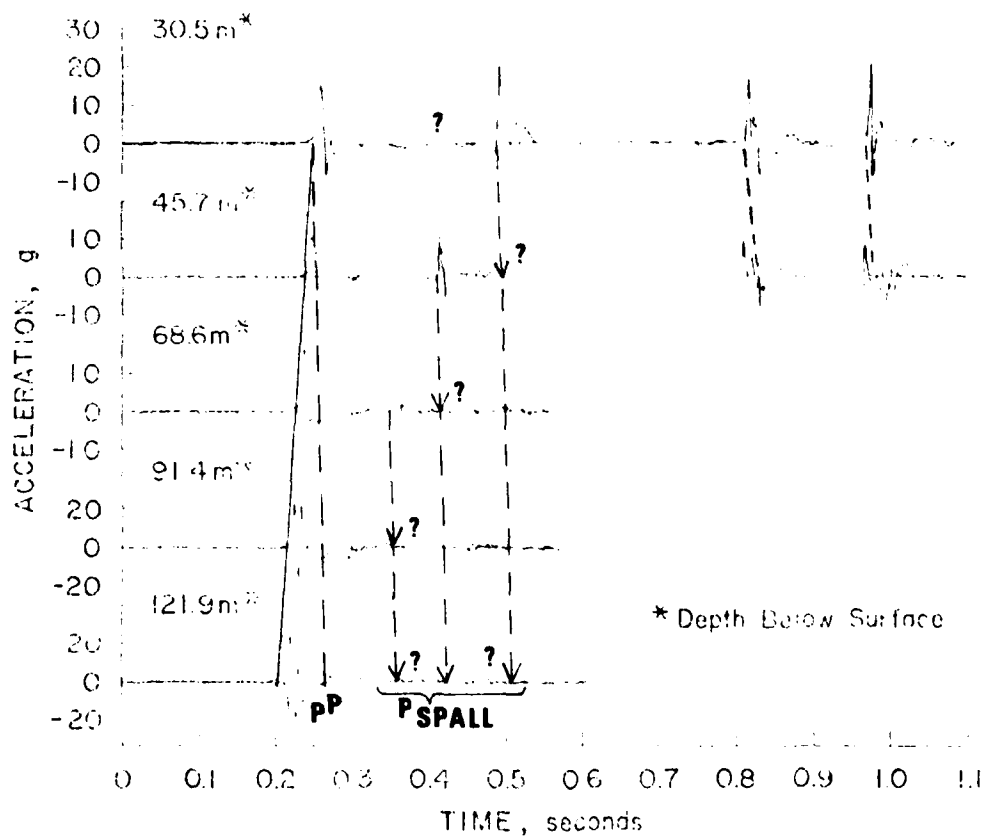
Figure 22.   Subsurface vertical accelerometer array data
for SALMON (Eisler, 1967).
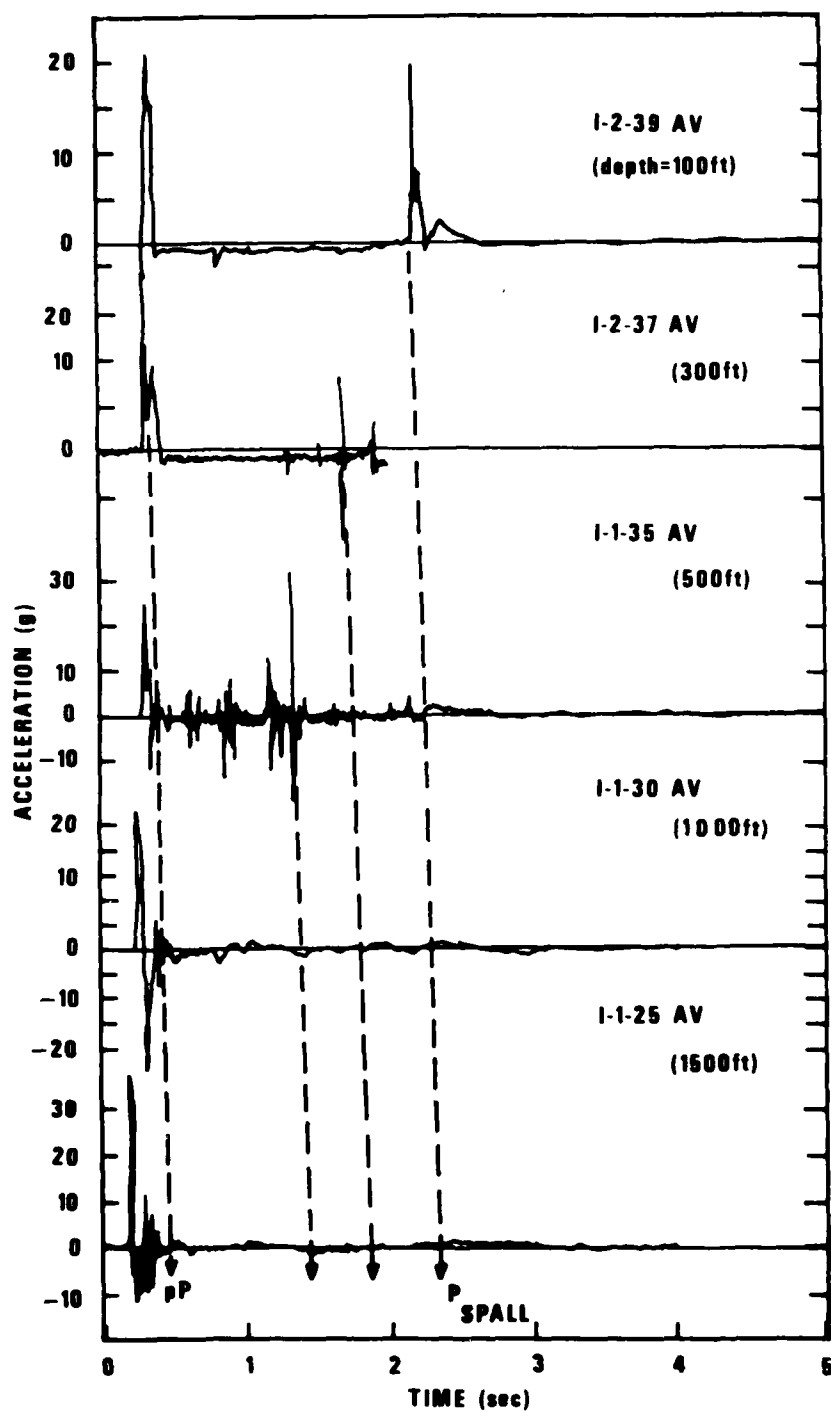
Figure 23. Subsurface vertical accelerometer array data for MILROW (Perret and Breding, 1972). Horizontal range = 299 feet.

- 49 -

If spall energy is large enough to be observed at teleseismic distances, then after closing each layer the spall signal should be propagating downward at the compressional velocity of the medium. Dashed lines in Figures 20 through 23 indicate expected downward flow of spall energy but none of these expected signals are observed. This situation exists because the spall signal for each layer closure is extended over a few tenths of a second, and each boundary is closing first at large ranges from the source and then near the shot hole where free-fall times are largest. If spall energy is significant, then spall signals observed at the surface should show extended periods of high amplitudes, but instead each signal is largely one pulse. Sources of spall signals are probably relatively low in energy and located close to the gauges. The spall signals only seem significant on surface records when compared to the initial acceleration pulse because the initial pulse has travelled a longer distance to the guage and is more highly attenuated than the spall signal. In fact, the subsurface vertical accelerometer array data show little if any spall energy leaving the source region. Thus spall appears to have little effect on m_b and M_s at teleseismic distances.

Subsurface observations of spall signals should be interpreted as observations of spall closures closest to that gauge and not observations of the first, and deepest, spall closures. Thus, the depths and vertical displacements of spall openings can only be determined with vertical subsurface arrays of accelerometers. Consequently, calculations of total energy in the closure of all spall layers depend upon subsurface data. P_{SPALL}-P times based on surface data are valid only for closure of the shallowest layer, which may not be the spall closure containing the most impact energy. The total height the ground surface is thrown is, then, the sum of multiple spall openings and it is not due to the first, and deepest, spall opening.

- 50 -

CONCLUSIONS

Sandia Laboratories near-field observations of spall on particle velocity data were used to estimate possible relationships between radius of spallation, thickness of spall, the maximum height attained by spall, shot depth of burial, and yield for 47 explosions. The following relationships were found

$\quad$ log (spall thickness) α 1/3 log (yield)

$\quad$ log (spall radius) α (1/3) log (yield)

$\quad$ log (maximum spall height) α .40 log (yield)

$\quad$ spall thickness α .10 shot depth of burial

Maximum spall height is inversely proportional to the scaled shot depth of burial but a best fit line through the data is poorly defined. Most scatter of data points in all comparisons is due probably to varying lithologies in in the source regions. Estimates of pP-p and P_{SPALL} - P times at teleseismic distances based upon surface accelerometer data are given in Table II. The spall arrival times are from 0.2 to 3.3 seconds after the main phase.

Using near-field displacement data, energies of the falling disc were calculated for each explosion and then compared to explosion energy that Perret (1972) calculated, or derived from the efficiencies found by Perret for various mediums. The explosions had spall energies ranging from 1 to 322 percent of the explosion energies. Thus, errors exist in assumptions used to calculate spall energy and/or explosion energy because spall energy cannot exceed that fraction of the explosion energy traveling upward into the spall region; for explosions in this study that fraction ranged from 1 to 37 percent. Relative spall energies compared to explosion energies for 42 NTS explosions located below the water table showed no relationship to M_s or strain release.

Subsurface vertical accelerometer data suggests that spall occurs over a range of depths, the deeper formations closing before the shallower layers. The large observed pulse of each spall closing is caused by the spall closure closest to that gauge. The surface accelerometer records indicate large spall energy, but the initial pulse has traveled a longer distance to the gauge and it has been more highly attenuated than the spall signal. The

- 51 -

principal error in the energy calculations was the assumption that one spall parting was largely responsible for observed surface displacements. Total energy, the sum of many spall closures, is probably much smaller than the spall energies calculated assuming that the first, and deepest, spall closure contained the most energy. Surface observations of spall have often been interpreted incorrectly by other investigators. Spall signals observed at the surface are observations of the spall closure closest to that gauge, not necessarily observations of the first, and deepest, spall closure. P_{SPALL}-P times calculated using surface data are for spall closest to the surface, which is the last spall to close and may not be the spall closure containing the most energy. Determining depths and vertical displacements of spall openings, and hence calculation of total energy in spall, depends upon observations from vertical subsurface accelerometer arrays. The total height the ground surface is thrown is the sum of multiple spall openings and it is not due to the first, and deepest, spall opening. The subsurface accelerometer data show little, if any, spall energy leaving the source region, suggesting that spall has little effect on m_b and M_s at teleseismic distances. Further investigations should accumulate more sub-surface accelerometer records and filter the data to enhance the lower frequencies which are more important in teleseismic analysis than the high frequency results shown in the literature.

REFERENCES

Chilton, F., Eisler, J., and H. Heubach, 1966. Dynamics of spalling of the Earth's surface caused by underground explosions, J. Geophys. Res., 71, 5911.

Eisler, J., 1967. Near-surface spalling from a nuclear explosion in a salt dome, J. Geophys. Res., 72, 1751.

Eisler, J., and F. Chilton, 1964. Spalling of the Earth's surface by underground nuclear explosions, J. Geophys. Res., 69, 5285.

Eisler, J., Chilton, F., and F. Sauer, 1966. Multiple subsurface spalling by underground nuclear explosions, J. Geophys. Res., 71, 3923.

Perret, W., 1968. Free-field particle motion from a nuclear explosion in salt, Part I, Vela Uniform Program, SALMON event, Sandia Laboratories, Report VUF-3012.

Perret, W., 1972. Seismic-source energies of underground nuclear explosions, Bull. Seism. Soc. Amer., 62, 763.

Perret, W., and D. Breding, 1972. Ground motion in the vicinity of an underground nuclear explosion in the Aleutian Islands: MILROW event, Sandia Laboratories, Research Report SC-ER-71-0668.

Springer, D., 1974. Secondary sources of seismic waves from underground nuclear explosions, Bull. Seism. Soc. Amer., 64, 581.

Viecelli, J., 1973. Spallation and the generation of surface waves by an underground explosion, J. Geophys. Res., 78, 2475.

von Seggern, D., and J. Gurski, 1976. m_s versus yield of underground nuclear explosions at the Nevada Test Sites, SDAC-TR-76-11, Teledyne Geotech, Alexandria, Virginia 22314.

Weart, W., 1962. Particle motion near a nuclear detonation in halite, Bull. Seism. Soc. Amer., 52, 981.

APPENDIX

Surface Particle Velocity Data
(Sandia Laboratories)

APPENDIX

Surface Particle Velocity Data
(Sandia Laboratories)

Explosion	Horizontal Range (m)	.5Δt (sec)	Peak Displacement (cm)
RAINIER	30	.25	10.62
	458	.14	1.60
ANTLER	149	.20	3.56
	301	.14	9.40
SHREW	0	.07	.71
MINK	9	.11	2.54
FISHER	23	.18	9.91
GNOME	402	.12	13.72
	805	.11	3.05
RINGTAIL	23	.14	3.81
STOAT	61	.14	4.32
DORMOUSE	46	.20	11.68
	198	.37	14.22
	366	.32	7.62
ARMADILLO	46	.22	21.34
	122	.44	8.64
	244	.15	3.56
HARDHAT	152	.31	5.59
	305	.15	15.49
CHINCHILLA I	15	.40	33.02
	84	.16	7.37
	168	.16	1.78
	335	.12	.51
PLATYPUS	15	.05	.86
	32	.04	.51
PAMPAS	15	.20	17.02
ERMINE	15	.03	.43

APPENDIX Continued

Surface Particle Velocity Data
(Sandia Laboratories)

Explosion	Horizontal Range (m)	$.5\Delta t$ (sec)	Peak Displacement (cm)
HOGNOSE	9	.17	8.89
	183	.45	5.33
	274	.32	8.89
CHINCHILLA II	15	.20	16.00
	69	.32	7.11
	137	.09	2.54
DORMOUSE PRIME	15	.22	20.32
AARDVARK	15	.45	55.88
	220	.26	33.02
	440	.25	19.56
	880	.18	8.13
RACCOON	15	.13	12.95
PACKRAT	15	.35	12.70
DAMAN I	15	.42	25.40
	132	.20	16.51
HAYMAKER	15	.59	43.18
	198	.25	12.95
	412	.26	11.18
	824	.21	6.35
CLEARWATER	0	.29	60.96
	211	.34	30.48
	364	.28	25.15
	668	.23	16.51
SHOAL	92	.17	57.40
	243	.15	21.34
	396	.19	32.00
	596	.13	4.57
SALMON	24	.17	34.04
	149	.20	25.91
	168	.17	25.91
	320	.11	9.14

APPENDIX Continued

Surface Particle Velocity Data
(Sandia Laboratories)

Explosion	Horizontal Range (m)	.5Δt (sec)	Peak Displacement (cm)
HANDCAR	15	.31	34.80
	122	.32	27.43
	213	.26	20.32
	427	.11	6.35
MUDPACK	15	.39	39.37
	46	.43	25.91
	91	.36	13.21
	168	.39	4.32
	259	.09	1.17
MERLIN	15	.25	11.61
	30	.23	13.21
	46	.22	11.91
	76	.22	12.70
	107	.22	11.02
	152	.20	10.92
	305	.14	4.93
	457	.11	1.70
DILUTED WATERS	15	.61	73.66
	76	.40	78.74
	152	.78	38.10
	229	.61	16.26
	500	.50	7.37
LONGSHOT	6	.72	224.28
	183	.56	90.42
	335	.47	91.19
	792	.20	30.99
	1219	.20	12.70
	1798	.12	5.08
PINSTRIPE	0	.55	61.47
	91	.48	61.21
	152	.33	42.93
	198	.11	17.27
DISCUS THROWER	15	.85	213.36
	46	.78	172.72
	122	.85	132.08
	488	.58	4.57
	1341	.21	1.27

A - 3

APPENDIX Continued

Surface Particle Velocity Data
(Sandia Laboratories)

Explosion	Horizontal Range (m)	.5Δt (sec)	Peak Displacement (cm)
PILEDRIVER	9	.65	233.68
	27	.73	254.00
	110	.66	271.78
	176	.65	243.84
	226	.75	248.92
	306	.60	157.48
	368	.48	142.24
	432	.43	106.68
	573	.40	66.04
	744	.21	22.86
	1372	.13	3.81
HALFBEAK	15	.91	480.06
	457	.40	157.48
	914	.36	35.56
	2134	.20	10.16
NEW POINT	6	.34	25.65
	30	.30	20.83
	46	.37	36.58
	91	.26	12.45
	198	.14	6.60
AGILE	13	.65	99.06
	91	.64	77.98
	457	.40	45.21
	905	.32	36.32
	1432	.22	8.89
COMMODORE	15	1.24	378.46
	91	1.21	99.06
	457	.88	125.48
	969	.28	38.10
SCOTCH	22	.44	89.41
	856	.32	25.91
	1206	.31	34.29
	2291	.17	8.13
DOORMIST	0	.35	73.66
	125	.28	33.02
	226	.18	35.56
	320	.15	7.37

Surface Particle Velocity Data
(Sandia Laboratories)

Explosion	Horizontal Range (m)	.5Δt (sec)	Peak Displacement (cm)
LANPHER	15	.83	152.40
	91	.78	167.64
	457	.70	63.50
	900	.30	28.45
	1437	.26	15.00
GASBUGGY	30	.20	17.09
	130	.20	15.06
	461	.17	8.66
	802	.12	6.91
FAULTLESS	26	.82	259.00
	152	.59	108.97
	457	.53	124.97
	1036	.44	89.92
	1828	.37	36.07
	3647	.27	28.96
KNOX	15	1.08	304.80
	91	1.02	276.86
	457	.35	58.93
BOXCAR	23	.93	327.66
	305	1.16	477.52
	914	.49	133.35
	2404	.36	33.02
	3813	.31	15.24
CYPRESS	0	.45	34.80
	125	.15	24.38
MILROW	76	.95	431.80
	573	.50	149.86
	1225	.37	78.74
	1354	.32	81.28
	1837	.27	27.94
	2010	.22	17.53